Journal of Sound and Vibration 537 (2022) 117211

Contents lists available at ScienceDirect

Journal of Sound and Vibration

journal homepage: www.elsevier.com/locate/jsvi

Machine learning non-reciprocity of a linear waveguide with a local nonlinear, asymmetric gate: Case of weak coupling

C. Wang [a,*], A. Mojahed [b], S. Tawfick [a,c], A. Vakakis [a]

[a] Department of Mechanical Science and Engineering, University of Illinois, Urbana USA
[b] Department of Mechanical Engineering, Massachusetts Institute of Technology USA
[c] The Beckman Institute for Advanced Science and Technology, University of Illinois, Urbana USA

ARTICLE INFO

Keywords:
Acoustic non-reciprocity
Nonlinear gate
Waveguide
Machine learning

ABSTRACT

This work considers the acoustics of an infinite, one-dimensional, linear waveguide composed of weakly coupled grounded oscillators, and incorporating a local nonlinear gate with cubic stiffness nonlinearity. A break of configurational symmetry is realized by the weak detuning of the two linear natural frequencies of the oscillators within the nonlinear gate. When harmonic excitation is applied to an oscillator of the waveguide, the synergy of nonlinearity and asymmetry at the local gate yields global effects in the acoustics, namely, in the form of strong non-reciprocity that is tunable with the frequency and intensity of the excitation. It is desirable to select the parameters for this system (such as mass, springs, nonlinear springs, etc.) to maximize its performance. Towards this objective, the nonlinear acoustics is studied by training two neural network (NN) simulators to evaluate (i) the harmonic contents of the transmitted waves through the nonlinear gate and (ii) the global non-reciprocity and transmissibility features of the waveguide. The training data is obtained by direct numerical simulations of the governing differential equations of motion. The predictions of the NN, which agree well with the direct simulations, drastically reduce simulation time, making practical the parametric study of the nonlinear acoustics and allowing for the detailed study the waveguide response at high-dimensional parametric domains. Using the NN, we demonstrate robust regions of non-reciprocal acoustic responses and achieve predictive design of the waveguide for maximum acoustic non-reciprocity. Indeed, it is shown that, when appropriately designed, the waveguide acts as an acoustic diode, allowing wave transmission only in one (preferred) direction and preventing wave propagation in the other direction. Moreover, depending on the system and excitation parameters, the non-reciprocally transmitted waves through the nonlinear gate can be either monochromatic or strongly modulated, i.e., possessing multiple frequency components. As a result, the non-reciprocal waveguide studied in this work may act either as a frequency converter or, conversely, as an acoustic diode with minimal frequency distortion of the transmitted waves. The developed machine learning approach is also applicable to a broad class of nonlinear waveguides with different configurations, asymmetries, and system properties, as well as in more than one dimensions.

* Corresponding author.
E-mail address: chongan2@illinois.edu (C. Wang).

https://doi.org/10.1016/j.jsv.2022.117211
Received 4 December 2021; Received in revised form 23 June 2022; Accepted 23 July 2022
Available online 25 July 2022

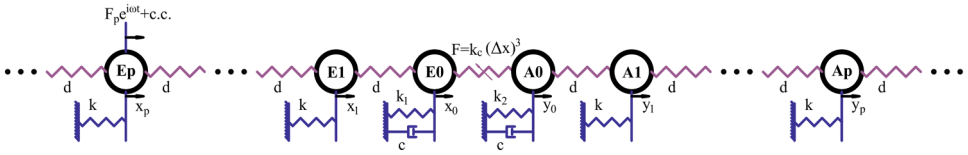

Fig. 1. Schematic of the linear weakly coupled waveguide with a local nonlinear gate.

1. Introduction

Reciprocity is a basic feature of linear time invariant (LTI) acoustic waveguides governed by Sturm-Liouville operators [1]. Basic ways of breaking reciprocity involve adding external biases [2,3,4], introducing time-variant properties [5] or imposing nonlinearity combined with some sort of asymmetry. Non-reciprocity in a waveguide violates the symmetry of the corresponding Green's function and introduces directional preference in wave transmission [6]. This motivates the study of non-reciprocal elements such as acoustic diodes [7], rectifiers [8], and frequency convertors [9].

Passive break of reciprocity in acoustic media is mostly associated with nonlinearity combined with asymmetry (disorder) [10]. A typical feature of the nonlinear acoustics is the dependence on amplitude, which makes a nonlinear waveguide tunable to energy. However, besides nonlinearity, spatial asymmetry is also necessary for realizing non-reciprocity [11], as shown in studies of nonlinear lattices [12], granular chains [13,14] and granular-solid interfaces [15]. Besides spatially extended (global) nonlinearities, non-reciprocity in linear waveguides may be achieved also through local nonlinear, asymmetric elements which are simpler and easier to fabricate; examples of such elements are vibro-impactors [16], bilinear oscillators [9], or cascades of hierarchical nonlinear oscillators [17].

In this work, we propose a new, relatively simple, and highly effective design for inducing controllable non-reciprocity in an otherwise LTI acoustic waveguide, locally augmented by an asymmetric, nonlinear gate. A single harmonic excitation with fixed amplitude and frequency is applied at an arbitrary constituent oscillator of the infinite waveguide. We show that the resulting locally augmented waveguide supports rich acoustics that are fully tunable with energy, and, more important, it may exhibit strong break of acoustic reciprocity (i.e., directed wave transmission in a preferential direction) with minimal structural modification in the local nonlinear gate.

The infinite LTI waveguide is assumed to have weak coupling between its constituent oscillators (yielding a single narrow pass band in the frequency domain), whereas, both nonlinearity and asymmetry are embedded in the local gate, which consists of two nonlinearly coupled oscillators with weakly detuned linearized natural frequencies. We analytically and numerically show that the nonlinearity and weak detuning of the *local* gate give rise to various types of *global* non-reciprocal acoustics, either with or without frequency distortion of the transmitted waves through the gate. Due to the high dimensionality of the design parameter space and the high complexity of the nonlinear acoustics, it is challenging and impractical to optimize the non-reciprocal performance by numerically integrating the governing differential equations of motion; rather a numerical approach based on machine learning is employed to study efficiently the nonlinear acoustics. Machine learning has been used to predict the responses of complex physical systems [18,19,20], and the resulting machine learning models (simulators) drastically reduce the computational effort required to predict the responses of high-dimensional systems or perform multi-task optimization in high-dimensional parameter spaces. In the machine learning model, the system and excitation parameters are considered as input variables, whereas the performance objective (in this case the achieved non-reciprocity in the gated waveguide) or the acoustical responses are regarded as output variables. Neural net (NN) simulators are created and trained to this end, that predict a set of outputs given arbitrary inputs in high-dimensional parameter domains. Since the trained NN simulators are much more efficient compared to direct numerical integrations of the governing nonlinear ordinary differential equations of motion, they are efficacious for numerically optimizing and predictively designing the considered waveguide for optimal non-reciprocity and desirable frequency conversion (or absence of) in the transmitted waves through the local gate.

This work is structured as follows. In Section 2, we introduce the mathematical formulation of the nonlinear acoustical problem. Two types of transmitted waves through the local gate are considered, namely monochromatic or strongly modulated. In Section 3, we create a NN model to predict the harmonic content of the acoustic response, which informs the design of the non-reciprocal gated waveguide for controllable frequency conversion (or absence of frequency distortion) of the transmitted waves through the gate. In Section 4, we create an additional NN model that directly predicts the performance of the waveguide as acoustic diode from two perspectives, namely, transmissibility and non-reciprocity; this model is used to perform optimization studies of waveguide performance. Lastly in Section 5, we provide a brief synopsis of the overall approach and the main findings of this work and discuss some possible further extensions of the method and applications.

2. The weakly coupled linear waveguide incorporating a local nonlinear, asymmetric gate

We consider the linear acoustic waveguide shown in Fig. 1, composed of two identical semi-infinite sub-waveguides connected through a local nonlinear gate. Each semi-infinite sub-waveguide consists of identical linear grounded oscillators, denoted E_n on the left side and A_n on the right side, with next-neighbor coupling through weak linear springs. The nonlinear gate is composed of two linear oscillators with identical masses but weakly detuned grounding stiffnesses and hence detuned natural frequencies; these

oscillators are coupled through an essentially nonlinear (i.e., non-linearizable) cubic stiffness. This is the only (local) nonlinearity of the waveguide, whereas the grounding detuning breaks the configurational symmetry. The only (weak) viscous damping of the waveguide is located at the nonlinear gate, as this ensures faster convergence to steady state of the response. The waveguide is excited by a single harmonic force applied to an oscillator of either one of the semi-infinite sub-waveguides (in the following analysis it is assumed that the excitation is applied to the $p-th$ oscillator of the left part of the waveguide E_p, cf. Fig. 1). For simplicity, the sub-waveguide where the excitation is applied is designated as the "upstream" one, and the other as the "downstream" one. Accordingly, the oscillators of the upstream (downstream) sub-waveguide are designated as $E_n,\ n=1,2,\ldots$ ($A_n,\ n=1,2,\ldots$), where the leading oscillators E_1 and A_1 are the ones coupled to the local nonlinear gate. Moreover, the oscillators comprising the nonlinear gate are designated as E_0 and A_0, where E_0 is coupled to the upstream sub-waveguide and A_0 to the downstream one (cf. Fig. 1). Then, the equations of motion of the gated waveguide are given by,

$$\begin{aligned}
&m\ddot{x}_0 + c\dot{x}_0 + k_1x_0 + k_c(x_0-y_0)^3 + d(x_0-x_1) = 0\\
&m\ddot{y}_0 + c\dot{y}_0 + k_2y_0 + k_c(y_0-x_0)^3 + d(y_0-y_1) = 0\\
&m\ddot{x}_n + kx_n + d(x_n-x_{n-1}) + d(x_n-x_{n+1}) = F_p\mathrm{e}^{\mathrm{i}\omega t}\delta(n-p) + \mathrm{cc},\ n>0\\
&m\ddot{y}_n + ky_n + d(y_n-y_{n-1}) + d(y_n-y_{n+1}) = 0,\ n>0
\end{aligned} \tag{1.1}$$

with all the initial conditions being equal to zero and $\mathrm{i}=(-1)^{1/2}$. In (1.1) x_0 and y_0 denote the displacements of the oscillators E_0 and A_0 of the nonlinear gate, x_n and y_n the displacements of the upstream and downstream oscillators E_n and A_n, respectively, t the time variable, and overdot the differentiation with respect to time. Regarding the system properties of the constituent oscillators, m denotes the mass, k and d the grounding and coupling linear stiffnesses, respectively, k_c denote the cubic nonlinear stiffness of the gate, and k_1, k_2, c_1, c_2 the stiffnesses and viscous damping coefficients of the two oscillators of the nonlinear gate, respectively. The only non-homogeneous term in (1) denotes the harmonic excitation applied to the upstream oscillator E_p, with F_p being the excitation amplitude and ω the excitation frequency. Lastly, $\delta(\cdot)$ is the Dirac function and (cc) denotes the complex conjugate pairs.

Introducing the following re-scalings,

$$\omega_0=\sqrt{k/m},\ \tau=\omega_0 t,\ \widehat{d}=\frac{d}{k},\ \widehat{d}_c=\frac{k_c}{k},\ \widehat{k}_1=\frac{k_1}{k},\ \widehat{k}_2=\frac{k_2}{k},\ \widehat{c}=\frac{c}{\sqrt{mk}},\ \widehat{F}_p=\frac{F_p}{k},\ \widehat{\omega}=\frac{\omega}{\omega_0}$$

the equations of motion are normalized as follows:

$$\begin{aligned}
&x_0'' + \widehat{c}x_0' + \widehat{k}_1x_0 + \widehat{d}_c(x_0-y_0)^3 + \widehat{d}(x_0-x_1) = 0\\
&y_0'' + \widehat{c}y_0' + \widehat{k}_2y_0 + \widehat{d}_c(y_0-x_0)^3 + \widehat{d}(y_0-y_1) = 0\\
&x_n'' + x_n + \widehat{d}(x_n-x_{n-1}) + \widehat{d}(x_n-x_{n+1}) = \widehat{F}_p e^{\mathrm{i}\widehat{\omega}\tau}\delta(n-p) + \mathrm{cc},\ n>0\\
&y_n'' + y_n + \widehat{d}(y_n-y_{n-1}) + \widehat{d}(y_n-y_{n+1}) = 0,\ n>0
\end{aligned} \tag{1.2}$$

where prime denotes differentiation with the re-scaled time τ. The current study is performed subject to certain basic assumptions. First, it is assumed that the linear intra-waveguide coupling stiffnesses between neighboring oscillations are *weak*, so that $\widehat{d}=\varepsilon D$, where $0<\varepsilon\ll 1$ is the small parameter of the problem. Similarly, the coefficient of nonlinearity is assumed to be small and scaled as $\widehat{d}_c=\varepsilon\alpha D$.

Due to the weak coupling, the pass-band of the linear sub-waveguides is narrow. By imposing the Bloch condition $x(y)_n=\mathrm{e}^{\mathrm{i}\theta}x(y)_{n-1}$, we obtain the dispersion relation of the linear sub-waveguides,

$$x(y)_n'' + \left\{1+\widehat{d}\left(2-\mathrm{e}^{\mathrm{i}\theta}-\mathrm{e}^{-\mathrm{i}\theta}\right)\right\}x(y)_n = 0 \Rightarrow \Omega=\sqrt{1+2\varepsilon D(1-\cos\theta)} \tag{1.3}$$

where θ denotes the wavenumber and Ω denotes the frequency that corresponds to the wavenumber θ. The range of Ω given by (1.3) is the normalized frequency pass-band of the linear sub-waveguides. The frequency pass-band of the infinite linear waveguide is narrow and given by $[\omega_{lb},\omega_{ub}]=[1,\sqrt{1+4\widehat{d}}]=[1,1+2\varepsilon D]+O(\varepsilon^2)$, where ω_{lb} and ω_{ub} denote the lower frequency bound (corresponding to in-phase oscillations of the linear waveguide) and upper frequency bound (corresponding to out-of-phase oscillations of the waveguide), respectively. The narrowness of the pass band of the waveguide is crucial for the following analytical approximations, since it enables a slow-fast time scale partition of the acoustical responses. Note that only harmonic waves with frequencies within this pass band can propagate unattenuated through the linear waveguide, whereas for other frequencies the waves spatially decay and represent near-field responses; hence, *only narrowband wave packages (that is, having harmonics in the narrow pass band) can propagate*. Moreover, the two stop bands of the waveguide are realized in the frequency ranges $(0,\omega_{lb})$ – lower stop band, and $(\omega_{ub},\ \infty)$ – upper stop band. Accordingly, the excitation frequency should be selected in the pass-band of the waveguide and expressed as, $\widehat{\omega}=1+\varepsilon D(1+\sigma_f)$ with is $\sigma_f\in[-1,1]$, since otherwise no transmitted waves from the forcing site could propagate along the waveguide without attenuation. Also, the excitation amplitude is scaled as small, $\widehat{F}_p=\varepsilon A_pD$. Moreover, the viscous damping coefficient is assumed to be of the same (small) order of the coupling, $\widehat{c}=2\varepsilon\zeta D$, and the normalized detunings of the grounding stiffnesses of the two gate oscillators are assumed to be small, i.e., $\widehat{k}_{1,2}=1+\varepsilon D\sigma_{1,2}$. A final assumption is that the acoustics satisfy the condition of 1:1 resonance, that is, the responses of all oscillators share the same (fast) frequency. Accordingly, the normalized equations of motion are expressed in the following form:

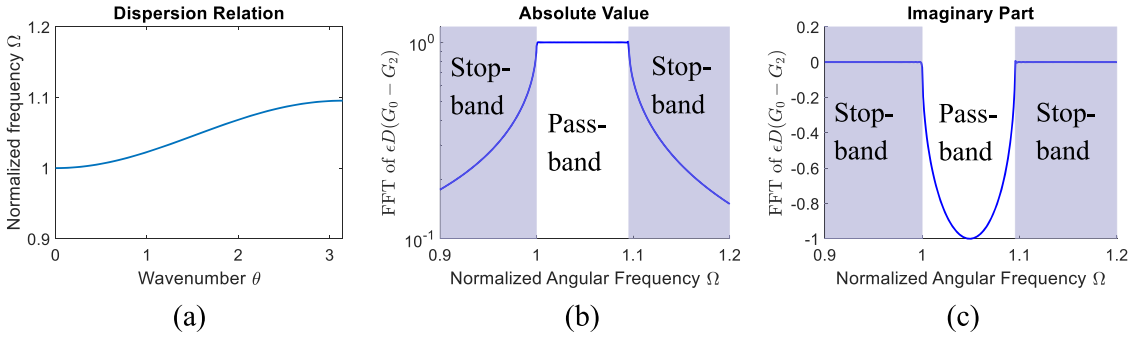

Fig. 2. Dispersion relation and transfer function for $\varepsilon = 0.05$ and $D = 1$: (a) Dispersion relation, (b) absolute value of the transfer function $|\mathscr{T}(\varepsilon D[G_0 - G_2])|$, (c) imaginary part of the transfer function $\mathrm{Im}(\mathscr{T}(\varepsilon D[G_0 - G_2]))$.

$$\begin{aligned}
&x_0'' + 2\varepsilon\zeta D x_0' + (1 + \varepsilon\sigma_1 D)x_0 + \varepsilon\alpha D(x_0 - y_0)^3 + \varepsilon D(x_0 - x_1) = 0\\
&y_0'' + 2\varepsilon\zeta D y_0' + (1 + \varepsilon\sigma_2 D)y_0 + \varepsilon\alpha D(y_0 - x_0)^3 + \varepsilon D(y_0 - y_1) = 0\\
&x_n'' + x_n + \varepsilon D(x_n - x_{n-1}) + \varepsilon D(x_n - x_{n+1}) = \varepsilon A_p D \mathrm{e}^{\mathrm{i}\left[1+\varepsilon D\left(1+\sigma_f\right)\right]\tau}\delta(n-p) + \mathrm{cc},\ n > 0\\
&y_n'' + y_n + \varepsilon D(y_n - y_{n-1}) + \varepsilon D(y_n - y_{n+1}) = 0,\ n > 0
\end{aligned} \tag{2}$$

We now proceed to a preliminary analytical exploration of the nonlinear response of the gated waveguide, considering the previous assumptions. To this end, we aim to analytically approximate the *monochromatic* response of the system by reducing the infinite number of differential equations (2) to an integro-differential reduced-order model (ROM). Noting that only source of nonlinearity is spatially confined to the gate, and that the overall structure of the waveguide is linear, the responses of all oscillators can be expressed in terms of the harmonic excitation and the responses x_0 and y_0 of the oscillators of the nonlinear gate through the following relations, which are based on the exact expressions of the Green's functions of the linear waveguide [21]:

$$\begin{aligned}
x_n &= \varepsilon D\left\{x_0(\tau) * [G_{n-1}(\tau) - G_{n+1}(\tau)] + \left[A_p \mathrm{e}^{\mathrm{i}\left[1+\varepsilon D\left(1+\sigma_f\right)\right]\tau} + cc\right] * \left[G_{p-n}(\tau) - G_{p+n}(\tau)\right]\right\}\\
y_n &= \varepsilon D y_0(\tau) * [G_{n-1}(\tau) - G_{n+1}(\tau)] \Rightarrow \mathscr{T}(y_n) = \mathscr{T}(y_0)\{\mathscr{T}(\varepsilon D[G_0 - G_2])\}^n
\end{aligned} \tag{3}$$

where $G_m,\ m = 1, 2, \ldots$ denotes the Green's function in the infinite waveguide [21,22] – whose explicit expression is given in Appendix A, $\mathscr{T}(\cdot)$ denotes the Fourier transform and $(*)$ denotes the convolution operator. From (3) we note that $\mathscr{T}(\varepsilon D[G_0 - G_2])$ denotes the transfer function of the responses between the adjacent oscillators of the downstream waveguide. In Fig. 2, we show the dispersion relation as well as the transfer function with $\varepsilon = 0.05$ and $D = 1$. From Fig. 2a, the pass-band is approximately $[1, 1.095]$. The magnitude of the transfer function between adjacent cells is shown in Fig. 2b, where the Discrete Fourier transform of the numerical time series is applied. In the frequency pass-band the magnitude of the transfer function is equal to unity, indicating that the transmitted wave propagates along the downstream sub-waveguide without attenuation. In the stop-band the magnitude of the transfer function is smaller than unity, indicating that the amplitude decays exponentially along the downstream sub-waveguide. The imaginary part of the transfer function is shown in Fig. 2c. Interestingly, the imaginary part of the transfer function is non-zero only in the pass-band.

Based on the relations (3), it is possible to express the infinite system of differential equations (2) in the following more compact set of just two nonlinear coupled integro-differential equations in terms of the responses x_0 and y_0 of the gate oscillators:

$$\begin{aligned}
&x_0'' + 2\varepsilon\zeta D x_0' + (1 + \varepsilon\sigma_1 D + \varepsilon D)x_0 + \varepsilon\alpha D(x_0 - y_0)^3 =\\
&\varepsilon^2 D^2 x_0 * (G_0 - G_2) + \varepsilon^2 D^2 \left[A_p \mathrm{e}^{\mathrm{i}\left[1+\varepsilon D\left(1+\sigma_f\right)\right]\tau} + \right] * \left(G_{p-1} - G_{p+1}\right)\\
&y_0'' + 2\varepsilon\zeta D y_0' + (1 + \varepsilon\sigma_2 D + \varepsilon D)y_0 + \varepsilon\alpha D(y_0 - x_0)^3 = \varepsilon^2 D^2 y_0 * (G_0 - G_2)
\end{aligned} \tag{4}$$

Note that system (4) is equivalent to the system (2), so it still possesses infinite degrees of freedom due to its integrodifferential terms. Also, to derive (4) the responses x_1 and y_1 in the two leading equations (4) were expressed in terms of x_0 and y_0 and the applied harmonic excitation through the corresponding Green's functions (cf. (3) and Appendix A).

System (4) governs the reflection and transmission of harmonic waves through the gate, as well as the wave scattering in the frequency (and wavenumber) domain due to the cubic stiffness nonlinearity at the gate. Hence, its study yields the *global* acoustic nonreciprocity features of the waveguide caused by the *local* nonlinearity and asymmetry at the gate; we note that in the absence of the gate the resulting linear acoustics of the waveguide is reciprocal. At this point we asymptotically analyze (4) by employing the method of multiple scales [23], expressing the oscillator responses in the following asymptotic series,

$$x_0(\tau) = x_{00}(\tau_0, \tau_1) + \varepsilon x_{01}(\tau_0, \tau_1) + O\left(\varepsilon^2\right), y_0(\tau) = y_{00}(\tau_0, \tau_1) + \varepsilon y_{01}(\tau_0, \tau_1) + O\left(\varepsilon^2\right) \tag{5}$$

where $\tau_0 = \tau$ and $\tau_1 = \varepsilon\tau$ are fast and slow time scales, respectively, in terms of the small parameter of the problem, ε. Substituting (5) into (4), expressing the time derivatives in terms of the new time variables τ_0 and τ_1, and considering only terms of $O(1)$, we obtain the

following leading-order approximations to the acoustical response of the gated waveguide:

$$\begin{aligned}&\frac{\partial^2 x_{00}}{\partial \tau_0^2}+x_{00}=0\Rightarrow x_{00}=X_{00}(\tau_1)\mathrm{e}^{\mathrm{i}\tau_0}+\mathrm{cc}\\&\frac{\partial^2 y_{00}}{\partial \tau_0^2}+y_{00}=0\Rightarrow y_{00}=Y_{00}(\tau_1)\mathrm{e}^{\mathrm{i}\tau_0}+\mathrm{cc}\end{aligned}\tag{6}$$

We note that by (6) we complexify the analysis and introduce slow-fast partitions of the solutions. Specifically, the leading-order approximations $x_{00}(\tau_0,\tau_1)$ and $y_{00}(\tau_0,\tau_1)$ are approximately expressed in terms of "slow" complex amplitudes (envelopes), $X_{00}(\tau_1)$ and $Y_{00}(\tau_1)$, that modulate the "fast" monochromatic oscillations, $\mathrm{e}^{\mathrm{i}\tau_0}$, with (normalized) fast frequency equaling unity. These amplitudes are determined by considering the next order approximation.

Before proceeding, however, to the $O(\varepsilon)$ approximations, as an intermediate step we express the Green's function as a slowly modulated oscillatory function with fast frequency close to unity,

$$G_n(\tau)=\frac{1}{2}(-\mathrm{i})^{n+1}J_n(D\tau_1)\mathrm{e}^{\mathrm{i}D\tau_1}\mathrm{e}^{\mathrm{i}\tau_0}+\mathrm{cc}+O(\varepsilon)\tag{7}$$

where $J_n(\cdot)$ denotes the Bessel function of the first kind and order n; details of this derivation are given in Appendix A. The complexification and slow-fast partition of the Green's function enables the continuation the asymptotic analysis in the complex domain. The system governing the $O(\varepsilon)$ approximations $x_{01}(\tau_0,\tau_1)$ and $y_{01}(\tau_0,\tau_1)$ is given in Appendix A. Substituting (6) and (7) into the $O(\varepsilon)$ set and eliminating secular terms (i.e., nonhomogeneous terms with fast frequencies equaling unity), we obtain the following *modulation or slow flow equations* that govern the slow evolutions of the leading-order approximations $X_{00}(\tau_1)$ and $Y_{00}(\tau_1)$,

$$\begin{aligned}&2i\frac{\partial X_{00}}{\partial \tau_1}+D(1+\sigma_1+2\mathrm{i}\zeta)X_{00}+3\alpha D(X_{00}-Y_{00})^2(\overline{X_{00}-Y_{00}})=\\&D^2\int_0^{\tau_1}\frac{1}{\mathrm{i}Ds}J_1(Ds)X_{00}(\tau_1-s)ds+D^2A_p\int_0^{\tau_1}\frac{p(-\mathrm{i})^p}{Ds}J_p(Ds)\mathrm{e}^{-\mathrm{i}D\sigma_f s}ds\mathrm{e}^{\mathrm{i}D\left(1+\sigma_f\right)\tau_1}\\&2\mathrm{i}\frac{\partial Y_{00}}{\partial \tau_1}+D(1+\sigma_2+2\mathrm{i}\zeta)Y_0+3\alpha D(Y_{00}-X_{00})^2(\overline{Y_{00}-X_{00}})=D^2\int_0^{\tau_1}\frac{1}{\mathrm{i}Ds}J_1(Ds)Y_{00}(\tau_1-s)ds\end{aligned}\tag{8}$$

where overbar denotes complex conjugate. These equations can be written in more compact form by introducing the transformations $\widetilde{X}_{00}=X_{00}/A_p$, $\widetilde{Y}_{00}=Y_{00}/A_p$ and $\widetilde{\tau}=\tau_1 D$, yielding the following set of transformed slow flow equations:

$$\begin{aligned}&2\mathrm{i}\frac{\partial\widetilde{X}_{00}}{\partial\widetilde{\tau}}+(1+\sigma_1+2\mathrm{i}\zeta)\widetilde{X}_{00}+3\alpha A_p^2(\widetilde{X}_{00}-\widetilde{Y}_{00})^2(\overline{\widetilde{X}_{00}-\widetilde{Y}_{00}})-\int_0^{\widetilde{\tau}}\frac{1}{\mathrm{i}s}J_1(s)\widetilde{X}_{00}(\widetilde{\tau}-s)ds=\int_0^{\widetilde{\tau}}\frac{p(-\mathrm{i})^p}{s}J_p(s)\mathrm{e}^{-\mathrm{i}\sigma_f s}ds\mathrm{e}^{\mathrm{i}\left(1+\sigma_f\right)\widetilde{\tau}}\\&2\mathrm{i}\frac{\partial\widetilde{Y}_{00}}{\partial\widetilde{\tau}}+(1+\sigma_2+2\mathrm{i}\zeta)\widetilde{Y}_{00}+3\alpha A_p^2(\widetilde{Y}_{00}-X_{00})^2(\overline{\widetilde{Y}_{00}-\widetilde{X}_{00}})-\int_0^{\widetilde{\tau}}\frac{1}{\mathrm{i}s}J_1(s)\widetilde{Y}_{00}(\widetilde{\tau}-s)ds=0\end{aligned}\tag{9}$$

From (9), we notice that there are five independent bifurcation parameters, that is, the two frequency detuning parameters $\sigma_{1,2}$ of the gate oscillators, the normalized excitation frequency σ_f, the normalized damping coefficient ζ, and the normalized excitation amplitude αA_p^2. In this work, we focus on the steady-state solutions of (9) which are reached in the limit when $\widetilde{\tau}\to+\infty$ and the nonhomogeneous term in the first of equations (9) becomes monochromatic. Moreover, since the slow flow (9) is in the form of two integro-differential coupled nonlinear equations, it still possesses an infinite number of degrees of freedom, so to qualitatively study its steady state solutions it is necessary to distinguish between two general classes of responses.

This first class of steady state solutions are *monochromatic*, i.e., the original responses $x_0(\tau)$ and $y_0(\tau)$ of the gate oscillators possess only a single fast frequency equal to the excitation frequency. Clearly, one could regard this type of solutions as *fundamental resonances* of the waveguide. In this case, the steady state solutions of (9) are complex constants, $\widetilde{X}_{00}=A_{X_{00}}$ and $\widetilde{Y}_{00}=A_{Y_{00}}$, yielding the leading-order approximations for the steady state responses of the gate oscillators, $x_0(\tau)\approx A_{X_{00}}\mathrm{e}^{\mathrm{i}(1+\sigma_f)\varepsilon D\tau}+\mathrm{cc}$ and $y_0(\tau)\approx A_{Y_{00}}\mathrm{e}^{\mathrm{i}(1+\sigma_f)\varepsilon D\tau}$. In this case the time derivatives in (9) are set to zero, and, as shown later, the resulting nonlinear complex algebraic equations can be analytically solved in terms of $A_{X_{00}}$ and $A_{Y_{00}}$. Then, this procedure gives identical results to the method of harmonic balance.

In the second class of steady state solutions of (9) the responses $x_0(\tau)$ and $y_0(\tau)$ of the gate oscillators possess *multiple slow frequencies and a single fast frequency (equaling unity)*. In that case, if we assume that there are at least two slow frequency components, say $\mathrm{e}^{\mathrm{i}\sigma\widetilde{\tau}}$ and $\mathrm{e}^{\mathrm{i}(\sigma+\Delta\sigma)\widetilde{\tau}}$, the nonlinearity will automatically generate additional frequency components in the form, $\mathrm{e}^{\mathrm{i}(\sigma-\Delta\sigma)\widetilde{\tau}}$ and $\mathrm{e}^{\mathrm{i}(\sigma+2\Delta\sigma)\widetilde{\tau}}$, since $(\mathrm{e}^{\mathrm{i}\sigma\widetilde{\tau}})^2(\overline{\mathrm{e}^{\mathrm{i}(\sigma+\Delta\sigma)\widetilde{\tau}}})=\mathrm{e}^{\mathrm{i}(\sigma-\Delta\sigma)\widetilde{\tau}}$ and $(\mathrm{e}^{\mathrm{i}(\sigma+\Delta\sigma)\widetilde{\tau}})^2(\overline{\mathrm{e}^{\mathrm{i}\sigma\widetilde{\tau}}})=\mathrm{e}^{\mathrm{i}(\sigma+2\Delta\sigma)\widetilde{\tau}}$. Therefore, it is inferred that in the second class of solutions the steady state response involves a *countable infinity of equally spaced harmonics*. Based on these arguments we anticipate the existence of quasi-periodic (generically) or periodic steady state solutions for the gate oscillators possessing countable infinities of equally spaced

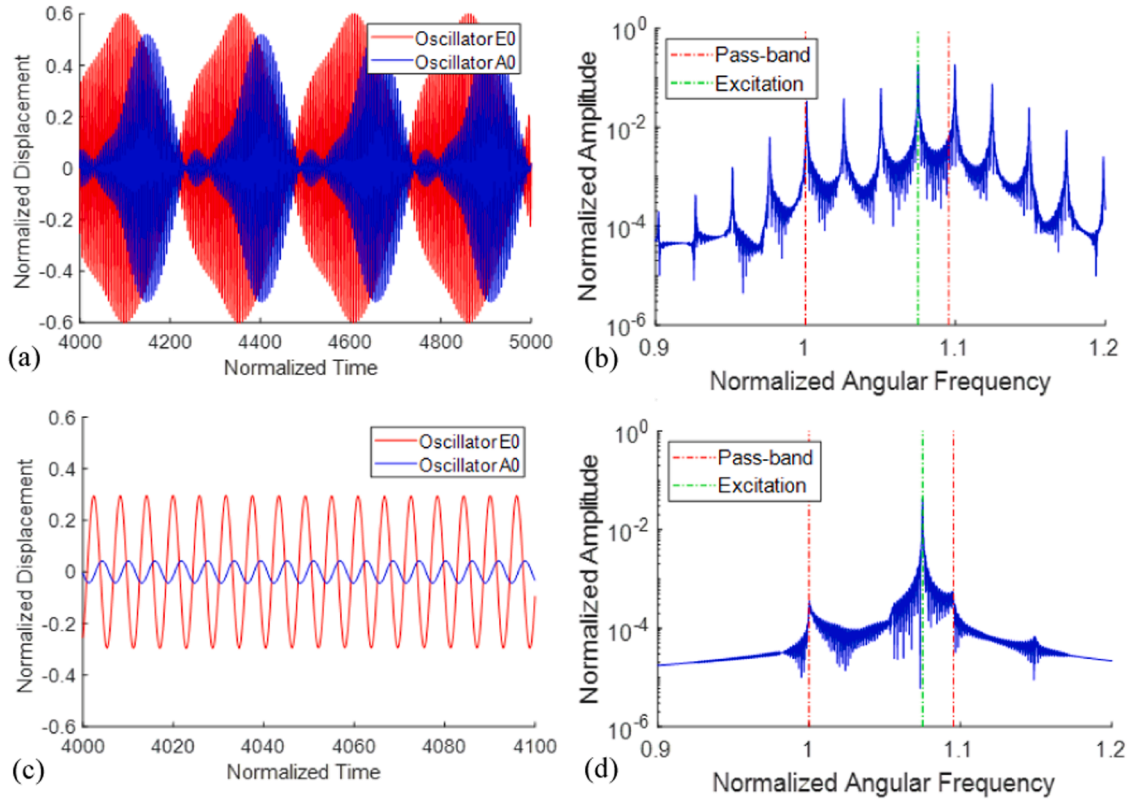

Fig. 3. Numerical simulations of the gated waveguide (2) at steady state: (a,b) Strongly modulated responses (SMRs) of the gate oscillators and Fourier transform of $y_0(\tau)$, respectively, for $(\sigma_1,\sigma_2) = (1,0)$, and (c,d) monochromatic responses of the gate oscillators and Fourier transform of $y_0(\tau)$, respectively, for $(\sigma_1,\sigma_2) = (0,1)$; the normalized excitation frequency (green dashed line) and the boundaries of the pass band (red dash lines) are indicated in (b,d).

harmonics centered to the excitation frequency; such solutions are referred to the literature as *strongly modulated solutions (SMRs)*. By substituting such an ansatz into the slow flow (9), we obtain a set of nonlinear algebraic equations with infinite degrees of freedom, which, however, is not analytically solvable.

To verify the analytical predictions, we numerically simulated the waveguide (2) composed of 1000 oscillators, focusing only on the responses of the two gate oscillators E_0 and A_0. The 4-th Runge-Kutta method is employed and the numerical simulations are performed by the MATLAB ode45 solver. The excitation was applied at the position $p = 4$, i.e., the 4^{th} oscillator from the gate E_4, and the simulation was carried out in the time window $0 \le \tau \le 15000$ to ensure that the steady state responses were not affected by wave reflections from the end boundaries. The system parameters were selected as, $\varepsilon = 0.05$, $D = 1$, $\alpha = 2$, $\zeta = 0.05$, $\sigma_f = 0.5$, $A_p = 0.25$, and $(\sigma_1,\sigma_2) = (1,0)$ or $(0,1)$; we note that inter-changing the values of the detunings σ_1 and σ_2 is equivalent to changing the site of the excitation from the $p-th$ oscillator of the left-half sub-waveguide to the $p-th$ oscillator of the right-half sub-waveguide. With $(\sigma_1,\sigma_2) = (1,0)$, the steady state responses of the gate oscillators are strongly modulated (cf. Fig. 3a), and correspond to the second class of predicted analytical solutions. This is clear by the Fourier spectrum of the response y_0 in Fig. 3b, which exhibits multiple equally-spaced peaks – a clear indication of a quasi-periodic response. Qualitatively different, monochromatic steady state responses of the gate oscillators are depicted in Fig. 3c for $(\sigma_1,\sigma_2) = (0,1)$, corresponding to the first class of analytically predicted responses. This is verified by the Fourier transform spectrum of the response y_0 in Fig. 3d where the steady response possesses a single peak coinciding to the excitation frequency. We note that the only difference between these two steady state responses is the interchange of the site of the harmonic excitation, form the left to the right sub-waveguide.

Furthermore, in Fig. 4 we compare the direct numerical simulations of system (2) for zero initial conditions to the (slowly varying) envelopes of the corresponding solutions predicted by the slow flow (9) again subject to zero initial conditions. Both SMRs and monochromatic responses are recovered by the slow flow, albeit for some phase differences for the case of SMRs (indicating an error in the analytical slow frequency of the modulations), which are due to the assumptions associated with the previous analysis, the most important of which are, (i) the existence of a single fast frequency in the responses, and (ii) the averaging operation (multiple-scale analysis) which, formally, is expected to hold up to time intervals of $O(1/\varepsilon)$ – for an improved approximation higher order averaging (multiple-scale expansion to higher orders) is required. Nevertheless, the analysis correctly predicts the amplitudes of the strong modulations in Figs. 4a,b and the envelopes of the monochromatic responses in Figs. 4c,d. Hence, the efficacy of the analytical model is verified.

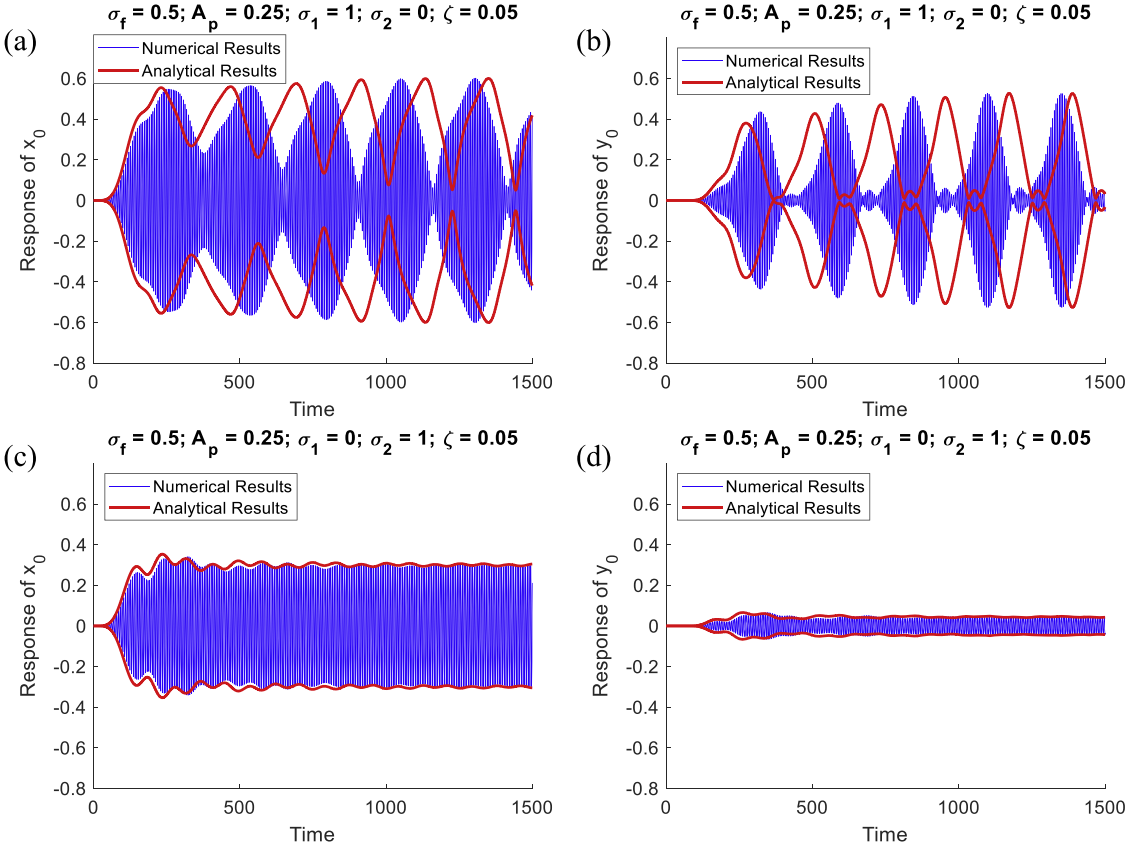

Fig. 4. Comparisons of direct numerical simulations of system (2) to the corresponding envelopes predicted by the slow flow (9): (a,b) Strongly modulated responses (SMRs) $x_0(\tau)$ and $y_0(\tau)$ of the gate oscillators, respectively, for $(\sigma_1, \sigma_2) = (1, 0)$, and (c,d) monochromatic responses $x_0(\tau)$ and $y_0(\tau)$, respectively, for $(\sigma_1, \sigma_2) = (0, 1)$; the system parameters are the ones used in Fig. 3.

The results depicted in Fig. 3 highlight the strong *acoustic non-reciprocity* of the gated waveguide, which is solely due to the local nonlinearity and asymmetry of the gate. Note that in the absence of the local nonlinear and asymmetric gate, the acoustics of the waveguide is fully reciprocal, in the sense that applying a harmonic excitation at oscillator E_p (source) and measuring the resulting response of oscillator A_p (receiver), one obtains an identical response if the sites of the source and the receiver are interchanged, that is, if the same harmonic excitation is applied at oscillator A_p (source) and the response is measured at oscillator E_p (receiver). Considering now the gated waveguide, as shown in Fig. 3, flipping the positions of the source and receiver is equivalent to flipping the values of the detuning parameters σ_1 and σ_2 in system (2); this change is sufficient to introduce strongly non-reciprocal steady state responses. The non-reciprocity of the gated waveguide will be the focus of the following study, where a machine learning approach will be adopted to make feasible the required load of numerical simulations.

3. Machine learning for predicting the steady state acoustics

From the analysis and results of Section 2, the non-reciprocal steady acoustics resulting from inter-changing the source and receiver sites of the harmonic excitation exhibits two main features, namely, a significant disparity in the response amplitudes as well as the corresponding frequency spectra. Having the aim to maximize (in some sense) acoustic non-reciprocity in the gated waveguide, it is necessary to investigate the relation between non-reciprocity, and the gate asymmetry and nonlinearity. Moreover, given the limitations of the analytical predictions and the computational demand of direct numerical simulations, we resort to machine learning, and specifically to NN, to explore the non-reciprocal features of this acoustical system.

We start by quantifying the non-reciprocity of the downstream steady state acoustics. Current literature [24,11,25] mainly focuses on quantifying non-reciprocity in transient acoustics through time series analysis, however, here we focus instead on the transmitted energy downstream. Indeed, considering a harmonic excitation applied at oscillator E_p, the energy transmitted to the downstream sub-waveguide can be estimated by the power transmitted from the gate oscillator A_0 to its neighboring oscillator A_1,

$$E_{down} = \int_0^T \varepsilon D(y_0 - y_1)\dot{y}_1 dt \tag{10}$$

where T denotes the simulation time window. We note that y_1 is fully determined from y_0 through the convolution relation (3). Hence, we can define the following energy-based non-reciprocity measure, δ,

$$\delta(T) = \log_{10}\frac{E_{down}(\sigma_1,\sigma_2,T)}{E_{down}(\sigma_2,\sigma_1,T)} \tag{11}$$

which is based on the downstream transmitted energy when the site of the harmonic excitation is switched from one sub-waveguide to the other. For a fully reciprocal system (i.e., in the absence of the gate), it holds that $y_0(\sigma_1,\sigma_2) = y_0(\sigma_2,\sigma_1)$ and $y_1(\sigma_1,\sigma_2) = y_1(\sigma_2,\sigma_1)$, so $\delta = 0$; this is a necessary condition for acoustic reciprocity. We note that the absolute value of δ quantifies the disparity of the energy transmission in orders of magnitude with the excitations applied on different sides. The left-to-right energy transmission overweighs the right-to-left energy transmission for positive δ, while the right-to-left energy transmission overweighs the left-to-right energy transmission for positive δ. Due to the symmetry, we only seek the parameters that enable non-reciprocal acoustics where left-to-right energy transmission is preferred, and therefore we seek large positive values of δ. A shortcoming, however, of the measure (11) is that it does not provide any information on the class of the steady state response, that is, if it is monochromatic or SMR, nor on its frequency content. To address this limitation, from (3) we express $y_1(\tau) = \varepsilon D y_0(\tau) * [G_0(\tau) - G_2(\tau)]$, substitute into (10), apply the Fourier transform and invoke the Parsevel-Plancherel theorem [26] to obtain the average power flow transmitted at steady state to the downstream sub-waveguide,

$$\lim_{T\to+\infty}\frac{E_{down}T}{T} = \mathrm{Re}\left(\varepsilon^2 D^2 \Big/ \pi \int_0^{+\infty} i\omega \mathscr{F}(G_0 - G_2)\mathscr{F}(y_0)\overline{\mathscr{F}(y_0)}d\omega\right) \tag{12}$$

where $\mathscr{F}(\cdot)$ denotes the Fourier transform and overbar the complex conjugate. It is shown in Fig. 2b that the imaginary part of $\mathscr{F}(G_0 - G_2)$ is non-zero only at frequencies inside the pass-band. Therefore, no energy is transmitted at the steady state for frequency components outside the pass-band. From (12) we note that the averaged power flow at steady state only depends on the amplitude of the frequency spectrum (and not on the phase). Hence, as the acoustics reach steady state, the downstream energy can be approximated based on the measure (12), which, in turn, is fully determined by the amplitude of the frequency response of the gate oscillator A_0.

For the non-reciprocity study of the steady state acoustics of the waveguide we investigate the effect of the detuning parameters (σ_1,σ_2) of the nonlinear gate. To this end, instead of computationally costly direct simulations of the governing nonlinear differential equations, we formulate a learnable simulator with the following two tasks. First, to map (relate) the detuning parameters (σ_1,σ_2) to the steady state frequency response $|\mathscr{F}(y_0)|$, and, then, based on the predicted frequency response $|\mathscr{F}(y_0)|$ to investigate the non-reciprocity measure δ and the downstream average power flow (12).

Staring from the first task, we note that $|\mathscr{F}(y_0)|$ is a continuous function in the frequency domain that involves *infinite degrees of freedom*. To simplify the learnable simulator, we create a reduced-order model (ROM) that approximates the frequency response

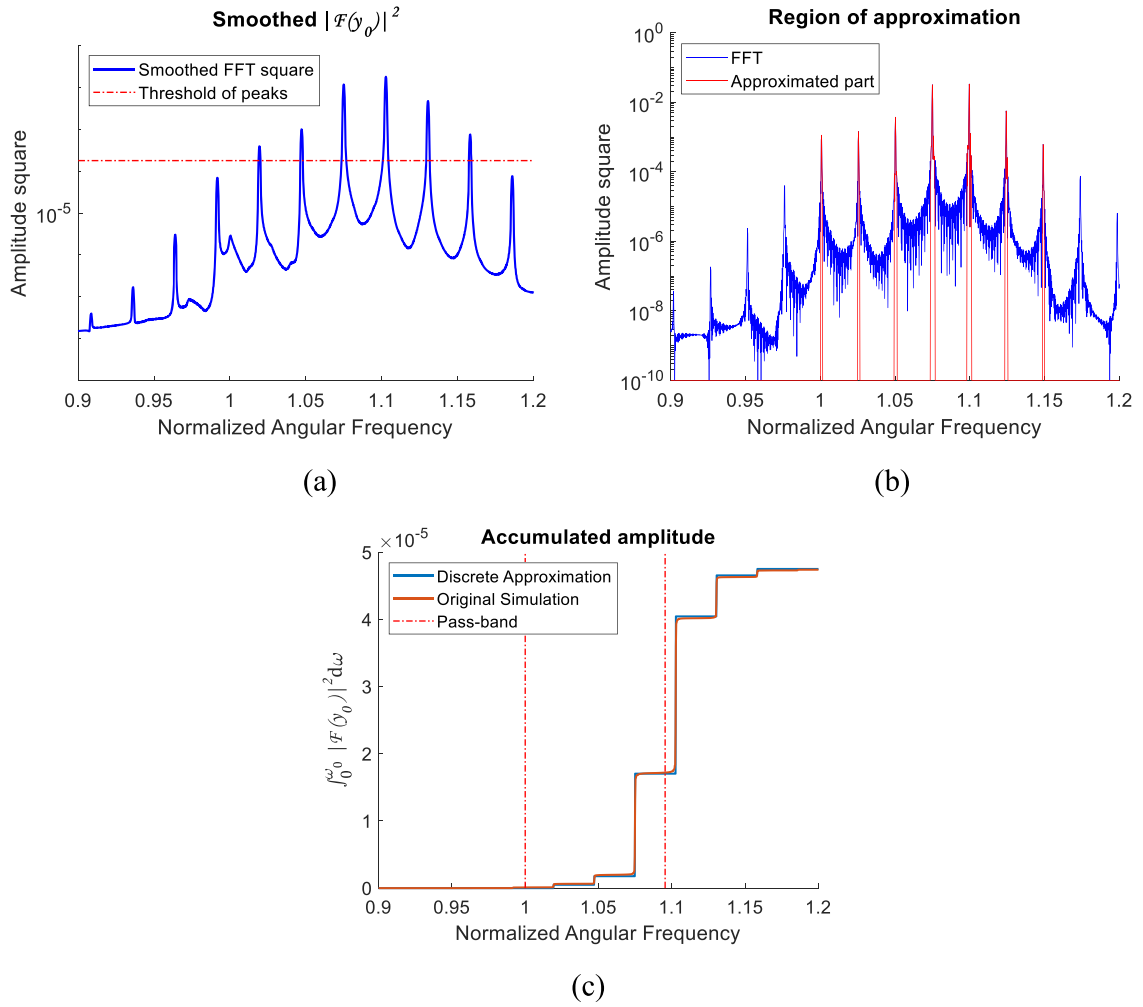

Fig. 5. ROM of the Fourier spectrum $|\mathscr{F}(y_0)|^2$ of the SMR depicted in Fig. 3b: (a) The smoothed frequency response $|\mathscr{F}(y_0)|^2$ and the amplitude threshold for the peaks, (b) approximated peaks considered in the ROM, and (c) comparison between the original Fourier spectrum and the ROM in terms of the accumulated frequency spectrum $\int_0^{\omega_0} |\mathscr{F}(y_0)|^2 d\omega$; the pass band of the linear waveguide is indicated in (c).

$|\mathscr{F}(y_0)|$ by a *finite-dimensional model*. The motivation for this comes from the plots of Figs. 3b and 3d which show that for both classes of steady state responses $|\mathscr{F}(y_0)|$ exhibits a varying number of distinct peaks in the pass band of the waveguide; clearly, only these peaks need to be accounted for in the ROM, since there are associated with downstream energy transfer in the downstream sub-waveguide – in fact, peaks outside the passband rapidly decay away from the local gate since they represent near-field responses that cannot transfer energy downstream. Therefore, it is reasonable to assume that the energy transmitted downstream is mainly localized at a finite number of distinct peaks, N. This enables us to approximate the continuous Fourier spectrum $|\mathscr{F}(y_0)|$ with the following approximate ROM composed of only N peaks localized at distinct frequencies:

$$|\mathscr{F}(y_0)|^2 \approx \sum_{i=1}^{N} \left\{ E^2(\omega_i)\delta(\omega-\omega_i) \right\} = \frac{1}{Fc} \sum_{i=1}^{N} \left\{ \int_{\omega_{lb,i}}^{\omega_{ub,i}} |\mathscr{F}(y_0)|^2 d\omega \delta(\omega-\omega_i) \right\},$$
$$Fc = \frac{\sum_{i=1}^{N} \int_{\omega_{lb,i}}^{\omega_{ub,i}} |\mathscr{F}(y_0)|^2 d\omega}{\int_0^{+\infty} |\mathscr{F}(y_0)|^2 d\omega} \times 100 \tag{13}$$

In this expression ω_i denotes the frequency of the $i-th$ peak, $E^2(\omega_i)$ the amplitude-squared of the $i-th$ peak, N the truncated total number of peaks considered in the ROM, and $\delta(\cdot)$ Dirac's function. In turn, $E^2(\omega_i)$ is approximated by integrating from a lower bound, $\omega_{lb,i}$, to an upper bound, $\omega_{ub,i}$, of the $i-th$ peak in the original (numerical) Fourier spectrum $|\mathscr{F}(y_0)|$; as discussed below, these bounds

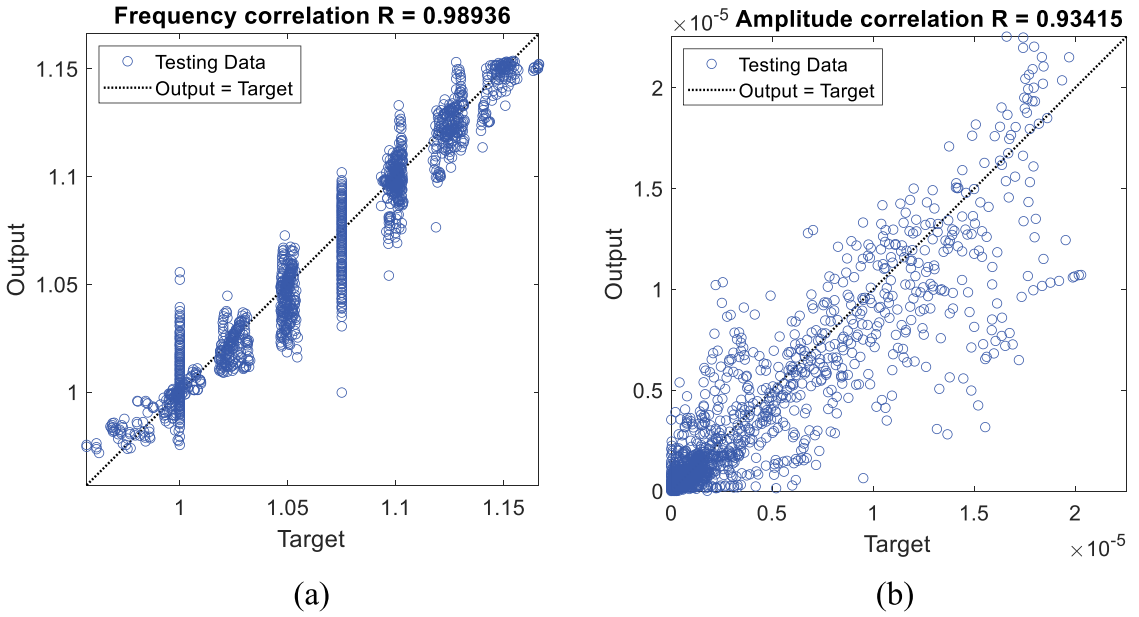

Fig. 6. Comparison between target and output of the NN for the testing set considered: (a) Frequencies ω_i, and (b) peak amplitudes-squared $E^2(\omega_i)$; the closer these data points are to the 45° line, the better is the performance (predictive capacity) of the NN.

are determined by specifying an amplitude threshold. Hence, by the ROM (13) $|\mathscr{F}(y_0)|^2$ is approximated by the linear superposition of a finite number of Dirac's functions located at the peaks, normalized by the factor *Fc* so that the integration over the entire frequency domain of the original transfer function $|\mathscr{F}(y_0)|^2$ and the approximate ROM are the same.

To construct (13) it is necessary to identify the frequency and the amplitude of each peak, the truncated number of peaks, *N*, taken into consideration, and the bounds $\omega_{lb,i}$ and $\omega_{ub,i}$ for each peak. To this end, we determined the number peaks of the ROM by, (i) smoothening (through a spline approximation) of the numerical discrete Fourier spectrum $|\mathscr{F}(y_0)|$, (ii) introducing an amplitude threshold to determine the number of peaks *N* of the ROM, as well as the bounds for each peak, and (iii) identifying the local maxima to determine the peak frequencies. As an example of the construction of the ROM, in Fig. 5 we approximate by (13) the SMR frequency spectrum depicted in Fig. 3b. The smoothed Fourier spectrum $|\mathscr{F}(y_0)|^2$ is plotted in Fig. 5a, and the amplitude threshold is set to 1% to identify the local maxima and the frequencies ω_i. From Fig. 5a, there are $N = 6$ local maxima, and these are considered for constructing the approximate ROM. The upper and lower bounds $\omega_{ub,i}$ and $\omega_{lb,i}$ for each peak of the ROM are evaluated as the intersections of the smoothed Fourier spectrum $|\mathscr{F}(y_0)|^2$with the amplitude threshold. In Fig. 5b the resulting ROM (red curve) is compared to the frequency response (blue curve). This enables the approximation of $|\mathscr{F}(y_0)|^2$ by the discrete function (13). To evaluate the accuracy of the ROM, in Fig. 5c we depict the square of the amplitude accumulated in the frequency domain, $\int_0^{\omega_0} |\mathscr{F}(y_0)|^2 d\omega$, for the original Fourier spectrum and the ROM. We note that the accumulated amplitude-squared behaves as a series of step functions, which validates the discrete approximation (13). Moreover, the normalization factor for the ROM is computed as = 96.7%, which shows that it approximates accurately the original frequency spectrum. Note that since the steady state energy transmitted downstream depends only on the frequency spectrum $|\mathscr{F}(y_0)|$, the discrete ROM (13) can be employed to accurately predict this quantity as well.

Once the discrete ROM (13) is constructed, we proceed to implement a machine learning methodology by building a learnable NN simulator that maps the system parameters of the gated waveguide to its steady state output for a range of system parameters. In what follows, the input variables are the gate detuning parameters σ_1 and σ_2, whereas the target and output variables are the frequencies and peak amplitudes, ω_i and $E(\omega_i)$, of the steady state responses, respectively. Once the frequency and peak amplitudes of the waveguide steady state responses are predicted, the resulting steady state energy transfer downstream could be computed. Extending the ROM of Fig. 5, the system and excitation parameters are fixed to the values, $\varepsilon = 0.05$, $\zeta = 0.05$, $\sigma_f = 0.5$, $D = 1$, $\alpha = 2$ and $A_p = 0.25$; these correspond to the results of Fig. 3, except for the gate detuning parameters σ_1 and σ_2 which are now varied. The NN is constructed and trained based on 1681 sets of data, which is created by performing direct numerical simulations of the governing equations of motion for the time window $\tau \in [0, 15{,}000]$, and parameters σ_1 and σ_2 in the range $[-2, 2]$ with an increment of 0.1. Details of the simulations are given in Appendix B. The simulation results show that the corresponding Fourier spectrum $|\mathscr{F}(y_0)|^2$ possess at most 10 peaks; such large number of peaks is realized for steady state SMRs – cf. Fig. 3b, whereas for monochromatic responses a single peak exists – cf. Fig. 3d. Details of the NN architecture and its training are given in Appendix B.

The efficacy of the NN is evaluated in Fig. 6 where we plot the target and output sets of the NN for the peak frequencies, ω_i, and the peak amplitudes-squared, $E^2(\omega_i)$. The target frequencies are compared to the NN predictions in Fig. 6a, and the output of the NN

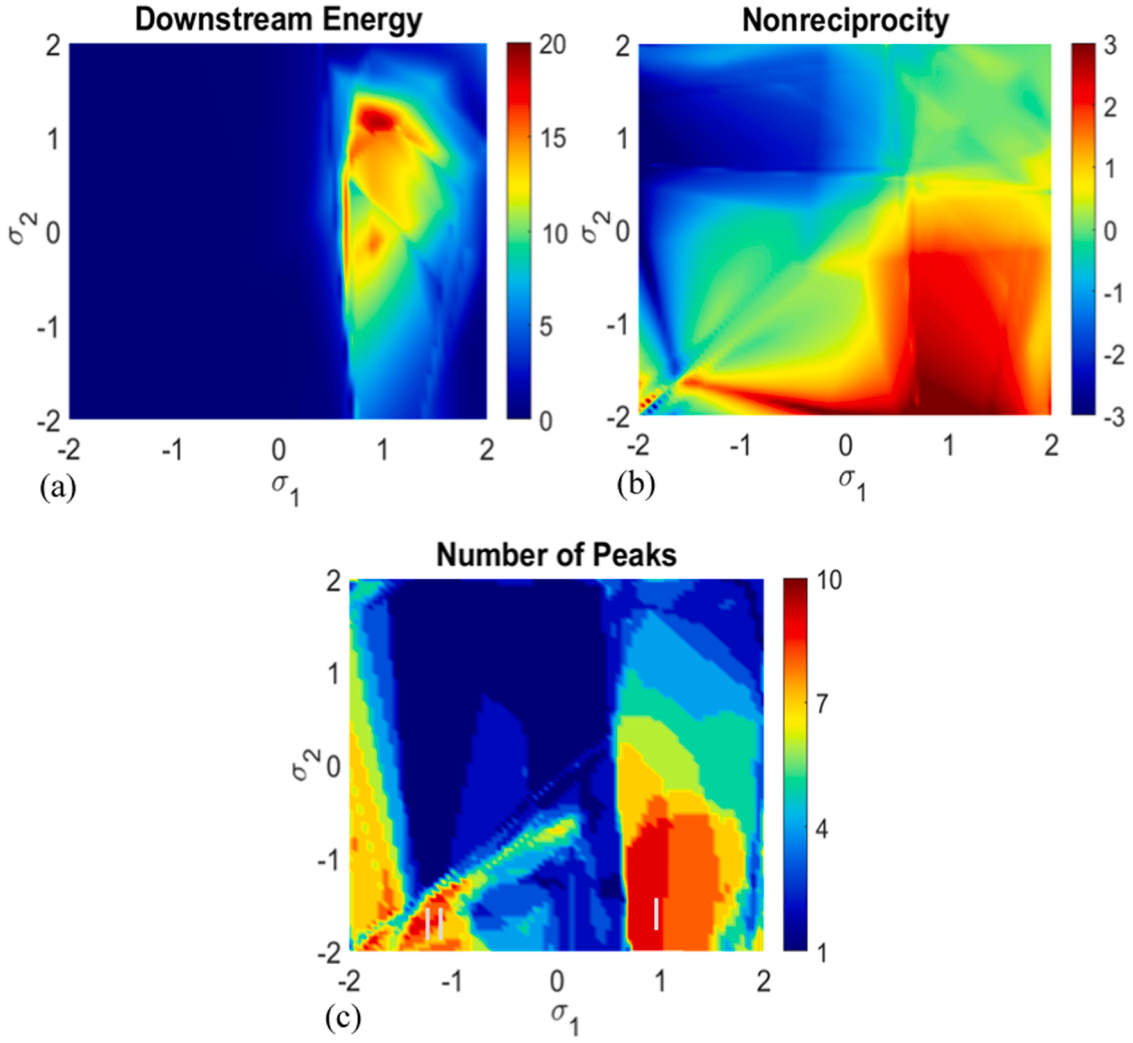

Fig. 7. Predicted results by the NN: Contour plots of (a) steady state energy (12) transmitted in the downstream sub-waveguide, (b) non-reciprocity measure (11), and (c) number of peaks; in (c) a single peak corresponds to monochromatic, and multiple peaks to SMRs in the steady state response of the gate oscillator $y_0(\tau)$. Two multi-peak regions are denoted as regions 'I' and 'II'.

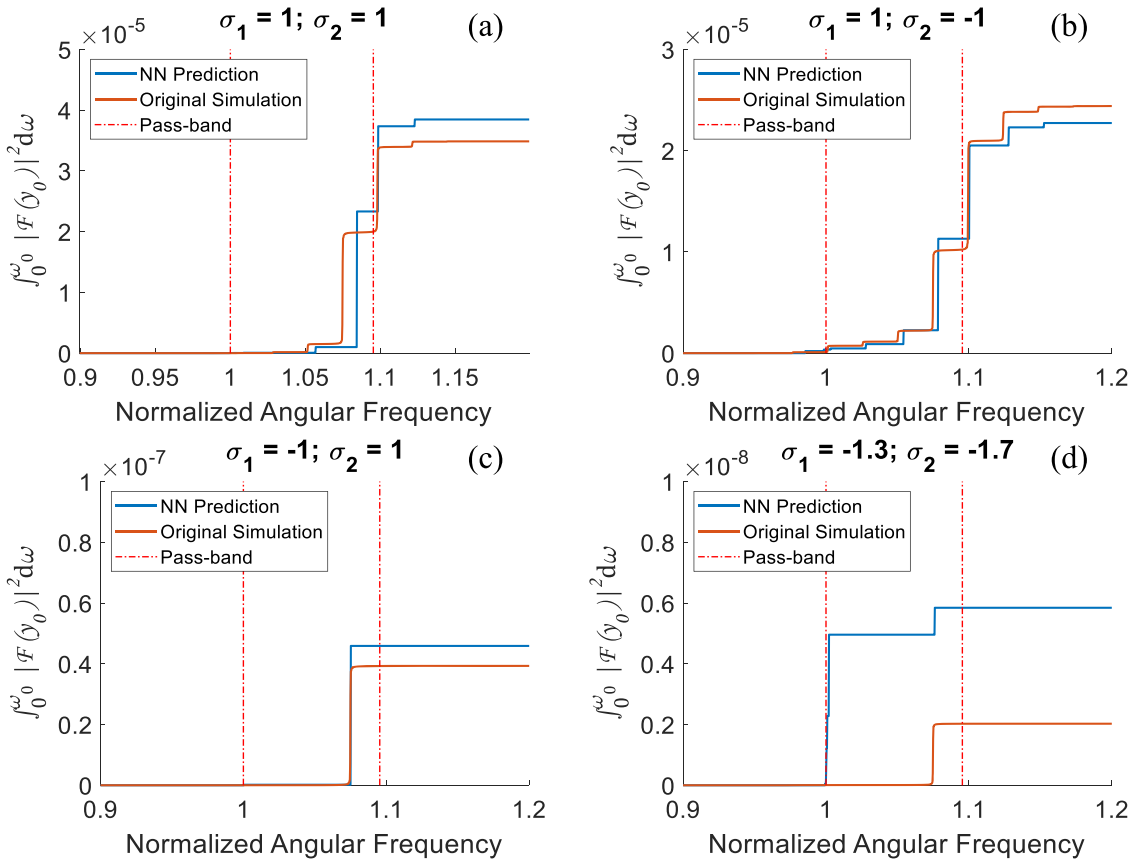

Fig. 8. Accumulated frequency spectra $\int_0^{\omega_0} |\mathscr{F}(y_0)|^2 d\omega$ predicted by the NN and direct numerical simulations: (a) $(\sigma_1,\sigma_2) = (1,1)$ – SMR, (b) $(\sigma_1,\sigma_2) = (1,-1)$ – SMR, (c) $(\sigma_1,\sigma_2) = (-1,-1)$ – monochromatic, and (d) $(\sigma_1,\sigma_2) = (-1.3,-1.7)$ – monochromatic; the passband of the linear waveguide is also indicated in these plots.

simulator is validated by the resulting correlation of ~ 0.99. The frequencies ω_i corresponding to the harmonics of the steady state SMR responses (e.g., Figs. 3a,b) are distributed approximately in the range $[0.95, 1.15]$ and cover approximately the pass-band. Similar efficacy of the NN simulator is inferred from the correlation results of Fig. 6b, where the correlation between target and output for the peak amplitudes-squared, $E^2(\omega_i)$, reaches ~ 0.93.

Having constructed the ROM for the Fourier spectrum $|\mathscr{F}(y_0)|$, we now proceed to the second (and main) task of the machine learning exercise, which is to make predictions of non-reciprocity in the gated waveguide, and of the energy transmitted in the downstream sub-waveguide at steady state. Based on the NN predictions of the frequencies and amplitudes of the identified peaks, we proceed to the prediction of downstream averaged power flow (12) and the non-reciprocity measure (11), with the results shown in contours of Fig. 7. In Fig. 7a, the contour depicts the downstream energy at $\tau = 15000$ by multiplying the predicted power flow (12) by the simulation window $T = 15000$. We note that the transmitted energy downstream reaches its maximum when both σ_1 and σ_2 are approximately equal to unity, and that high values of this measure are realized in the first and the fourth quadrants of the plot of Fig. 7a. Moreover, the downstream transmitted energy is asymmetric with respect to the diagonal $\sigma_1 = \sigma_2$, which leads to the strong non-reciprocity. In Fig. 7b, the contour depicts the non-reciprocity measure (11) based on the NN prediction of the downstream energy E_{down} at $T = 15000$. The maximum non-reciprocity is noted in the second and fourth quadrants. In fact, the non-reciprocity measure is anti-symmetric with respect to the diagonal $\sigma_1 = \sigma_2$, with the strongest non-reciprocity being observed mainly in the fourth quadrant of the contour measure plot of Fig. 7b, especially for $\sigma_1 > 0.5$, where the measure δ is close to 2; this means that in that region the downstream energy becomes two orders of magnitudes smaller if we flip the position of excitation and measurement. Note, however, that in the second quadrant of that plot the downstream transmitted energy is small, and so of no practical significance. Lastly, in Fig. 7c we consider the number of peaks predicted by the NN for varying values of (σ_1,σ_2) (with details available in Appendix B). We infer that maximum non-reciprocity in the gated waveguide is related to the greatest number of peaks in the fourth quadrant of the plot of Fig. 7c; whereas in the second quadrant of that plot we mainly observe a single peak in the Fourier spectrum of y_0, however, this parameter range is also associated with weak downstream energy transmission and is of no practical significance.

As in the plot of Fig. 5c we evaluate the accuracy of the predictions of the NN by computing he accumulated frequency spectrum

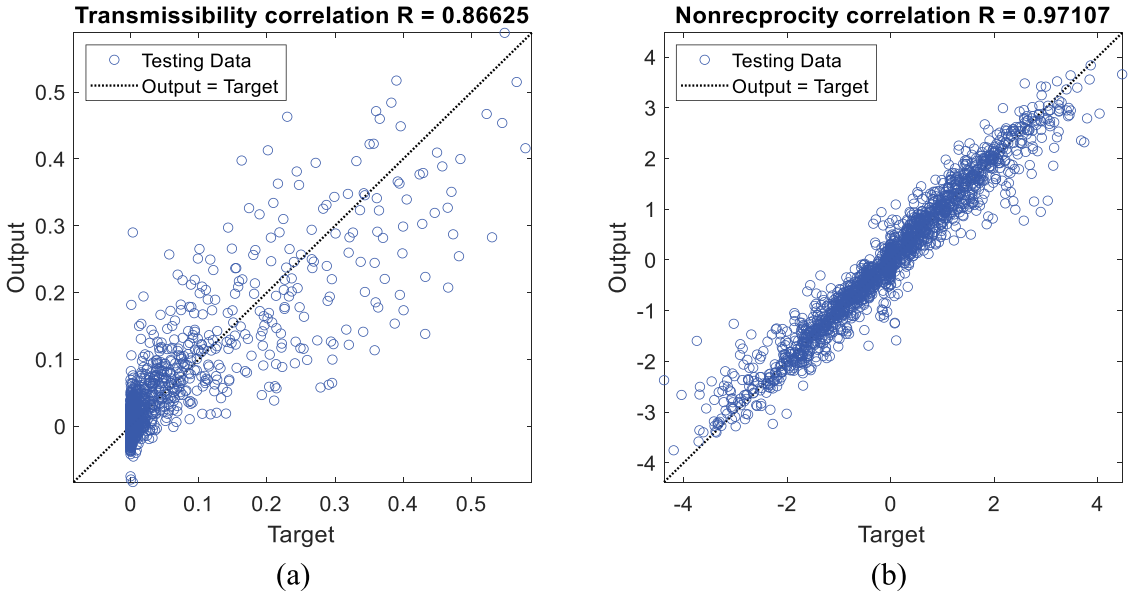

Fig. 9. Comparison between the target and output (prediction) of the first NN based on the coarse testing set: (a) Transmissibility η, and (b) Non-reciprocity measure δ.

$\int_0^{\omega_0} |\mathscr{F}(y_0)|^2 d\omega$ and comparing it with the result obtained by direct numerical simulations of the governing equations of motion. The results are depicted in Fig. 8 for four pairs of parameters (σ_1, σ_2) selected in the four quadrants of Figs. 7a-c. The cases $(\sigma_1, \sigma_2) = (1, 1)$ and $(1, -1)$ are shown in Figs. 8a and 8b, respectively, and both correspond to steady state SMRs (cf. Fig. 5a) and strong steady state energy transmission downstream; moreover, the NN outputs agree well with the simulations in terms of both peak amplitudes and frequencies. In Fig. 8c we depict the case $(\sigma_1, \sigma_2) = (-1, 1)$ where the NN manages to predict the monochromatic steady state response. Note, that in this case the accumulated frequency spectrum is about two to three orders of magnitude lower compared to the case $(\sigma_1, \sigma_2) = (1, -1)$; since the energy transmitted downstream is proportional to the square steady state amplitude, the non-reciprocity measure δ in this case should also be close to $-2 \sim -3$, which indeed is close to the NN prediction. Lastly, the accumulated frequency spectrum of Fig. 8d corresponds to $(\sigma_1, \sigma_2) = (-1.3, -1.7)$ and again corresponds to monochromatic steady state response (it corresponds to a region with a single peak in the third quadrant of Fig. 7c). This case yields the smallest steady state response among these cases, being 4 orders of magnitude smaller compared to the cases $(\sigma_1, \sigma_2) = (1, -1)$ or $(\sigma_1, \sigma_2) = (1, 1)$, and is a case where the NN prediction does not agree well with the direct simulation result. In particular, the NN predicts with multiple peaks, compared to the single peak shown in the numerical simulation; however, we notice that the absolute error between these results is small due to the weak response in this case. Since the mean square error is used as the objective function for minimization, it is in the same order with the responses, which explains the poor prediction of the NN in this case.

Considering the overall plot of Fig. 7c, the multi-peak area (corresponding to SMRs) is divided into two regions, namely, region I corresponding to $\sigma_1 > 0$, and region II with $\sigma_2 < 0$. In region I, the transmitted energy downstream is intense and the NN provide an accurate prediction. On the contrary, in region II, the transmitted energy is small, and, therefore, as discussed previously the SMRs predicted by the NN might be inaccurate. In general, the designed NN accurately predicts the steady state responses in regimes of strong downstream energy transmission, both in terms of frequencies and amplitudes, and thus paves the way for optimizing the performance of the waveguide in terms of maximum realized non-reciprocity. In the next section we will extend our machine learning based approach to predict parameter ranges of the gated waveguide for optimal performance, in the sense that both the non-reciprocal measure δ, and the steady state energy transmitted downstream are simultaneously optimized.

4. Performance optimization through machine learning

In this section, we create an extended machine learning model to map the system parameters to the performance of the gated waveguide, and then perform its optimization. In addition to the non-reciprocity and the downstream energy measures defined in Section 3, we are also interested in the transmissibility measure, that is, on the proportion of total energy induced in the upstream sub-waveguide that is eventually transferred to the downstream sub-waveguide. The transmissibility measure is defined as,

$$\eta = \frac{E_{down}(T)}{E_{input}(T)} = \frac{E_{down}(T)}{\int_0^T 2\varepsilon A_p D \dot{x}_p \cos\left[1 + \varepsilon D\left(1 + \sigma_f\right)\right] \tau d\tau} \tag{14}$$

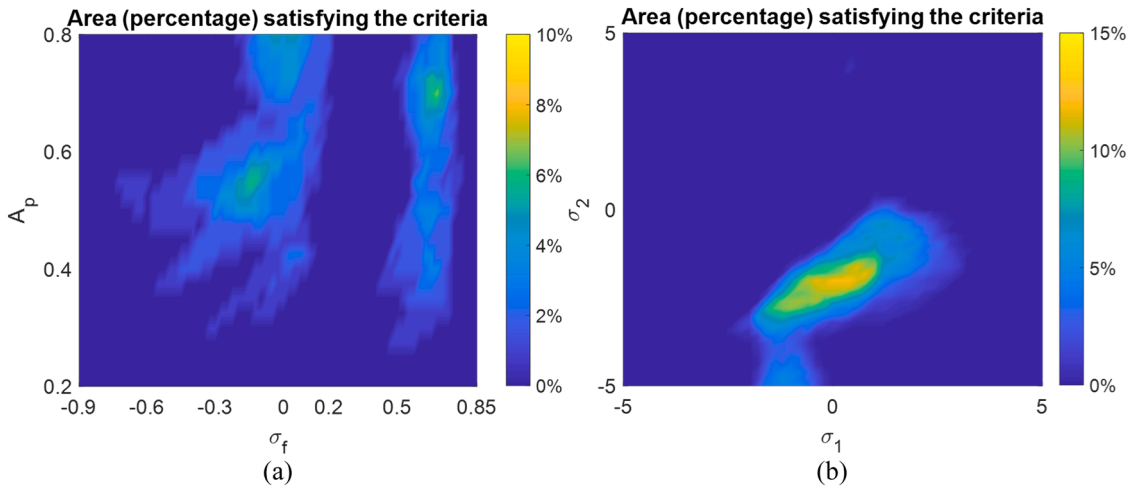

Fig. 10. Subregions of good performance based on the coarse dataset: (a) Detuning parameters (σ_1, σ_2) for given excitation parameters (σ_f, A_p), and (b) excitation parameters (σ_f, A_p) for given detuning parameters (σ_1, σ_2).

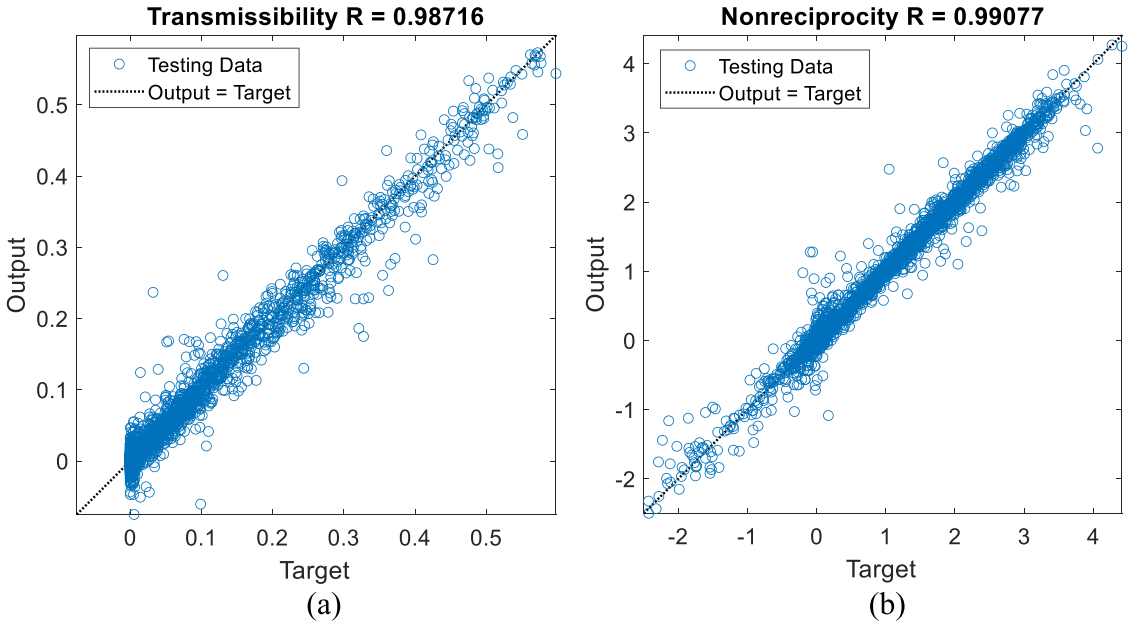

Fig. 11. Comparison between the target and output (prediction) of the second NN for the testing set: (a) Transmissibility measure, and (b) Non-reciprocity measure.

where E_{input} denotes the total input energy to the gated waveguide up to time T, which is equal to the work performed by the applied harmonic excitation, and E_{down} the energy transmitted to the downstream sub-waveguide up to time T. Accordingly we relate the performance of the gated waveguide with *non-reciprocal transmissibility* η, that is, we aim to design this system for maximum transmissibility downstream *and* negligible transmissibility in the reverse direction, i.e., when the site of the harmonic excitation is exchanged between the upstream and downstream sub-waveguides. Moreover, in optimizing performance we will extend the NN simulator to account not only for the detuning parameters σ_1 and σ_2, but also the excitation parameters σ_f and A_p. Hence, the learnable simulator will be extended to map the detuning and the excitation parameters $(\sigma_1, \sigma_2, \sigma_f, A_p)$ to the non-reciprocity measure δ and transmissibility measure η. In the following results the remaining parameters are kept fixed to the values, $\varepsilon = 0.05$, $\alpha = 2$, $D = 1$ and $\zeta = 0.05$.

The machine learning prediction is performed in two steps. In the first step, a "coarse" initial exploration is performed with a NN simulator that is created to roughly estimate the subregion of good performance from a large dataset. Then, to predict the performance more accurately, in the second step a finer study is performed through a second neural NN that is created for a more compact dataset

Table 1
Confusion matrix for assessing the predictive capacity of the second NN

Data points in the test set	Predicted condition			Performance
Actual condition	Data points $N = 2356$	Desirable	Undesirable	
	Desirable	TP = 101	FN = 14	Sensitivity: 0.878
	Undesirable	FP = 9	TN = 2232	Specificity: 0.996
				Precision: 0.918

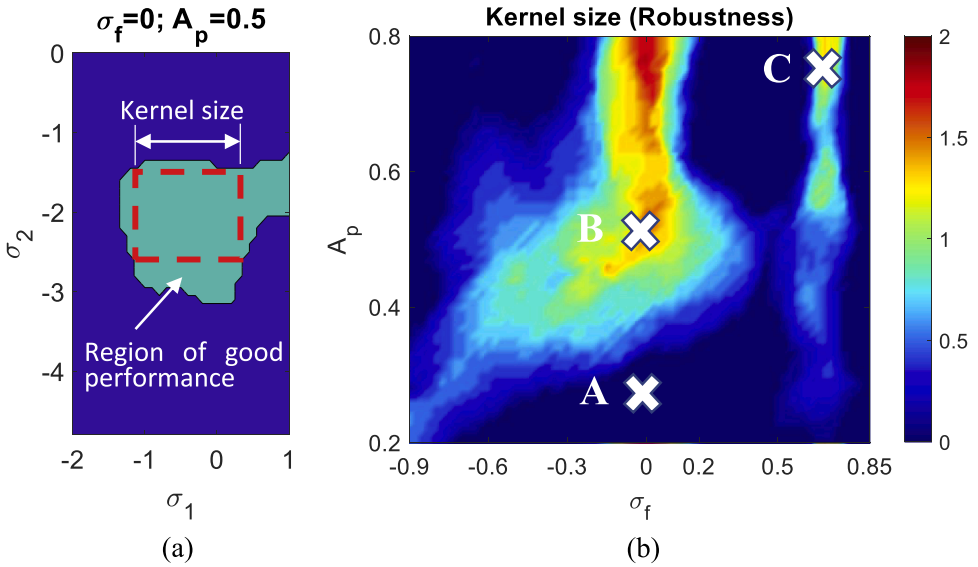

Fig. 12. Predicted regions of good performance by the NN: (a) In (σ_1, σ_2) plane for fixed $(\sigma_f, A_p) = (0.75, 0)$ with kernel shown, (b) contour plot of kernel size for varying (σ_f, A_p).

only from the subregion predicted at the first step. Both NN adopt the Rectified Linear Unit (ReLU) functions as activation functions for the hidden layers (cf. Appendix B), and their training is through the Levenberg-Marquardt algorithm based on the MATLAB deep learning toolbox.

The first NN is created based on simulations of the equations of motion from $\tau = 0$ to 15000 on a coarse grid dataset. The dataset considers values of σ_1 and σ_2 ranging from -5 to 5 with increment 1, and A_p from 0.2 to 0.8 with increment 0.15. Also, given that the normalized passband of the linear waveguide is $[1, \sqrt{1 + 4\varepsilon D}]$, we consider $\sigma_f \in [-1, 20\sqrt{1.2}\ -21] \approx [-1, 0.91]$ to ensure that the excitation frequency is located in the pass-band. However, when the excitation frequency is close to the boundary of the passband, the group velocity is close to zero which makes it difficult for the acoustics to reach the steady state; therefore, the coarse grid values of σ_f are selected as -0.9, -0.6, -0.3, 0, 0.2, 0.35, 0.5, 0.65 and 0.85 for the dataset generation. From this dataset, 50% is used for training, 15% for validation and 35% for testing. Each of the input and output variables is normalized in the range $[-1, 1]$ through a linear mapping, with the minimum mapped to 0 and the maximum to 1. Moreover, the first NN involves three hidden layers with 30 neurons per layer (cf. Appendix B).

The target values and predictions of the NN for the transmissibility and non-reciprocity measure are shown in Fig. 9 to evaluate its efficacy. We note that the NN can only predict the trend of the performance with low accuracy. Therefore, we still need to refine the grid dataset for a higher accuracy. Since we only focus on the subregion with high transmissibility and non-reciprocity, the second NN (for the finer data exploration) is created only based on the specific subregion with good performance predicted by the first NN. In this work, we consider the choice of parameters of the acoustic waveguide for good performance if it is satisfied that $\delta > 1$ for the non-reciprocity, and $\eta > 0.2$ for transmissibility; hence, we require that at least 20% of the input energy is propagating downstream (transmissibility), and that the difference between the waveguide responses when the excitation is switched between the two sub-waveguides is at least one order of magnitude (non-reciprocity). This yields a four-dimensional subregion of good performance, which is difficult to visualize. Instead, we first fix the excitation frequency and amplitude (σ_f, A_p) and consider the subregions of good performance in the (σ_1, σ_2) domain. The areas of these subregions are then computed and normalized by the total area of the (σ_1, σ_2) domain $[-5,5] \times [-5,5]$, and presented in Fig. 10a. We note that for varying values of (σ_f, A_p), there are two robust subregions of good performance; one is for σ_f being approximately in the range $[-0.6, 0.1]$ and A_p in $[0.3, 0.8]$, while the other is for σ_f ranging approximately in $[0.4, 0.8]$ and A_p in $[0.25, 0.8]$. In the complementary regions the non-reciprocity and/or the transmissibility do not meet the posed requirements for good performance regardless of the values of (σ_f, A_p) and (σ_1, σ_2). Similar contours for a subregion of good performance in the (σ_f, A_p) domain is plotted in Fig. 10b for varying (σ_1, σ_2).

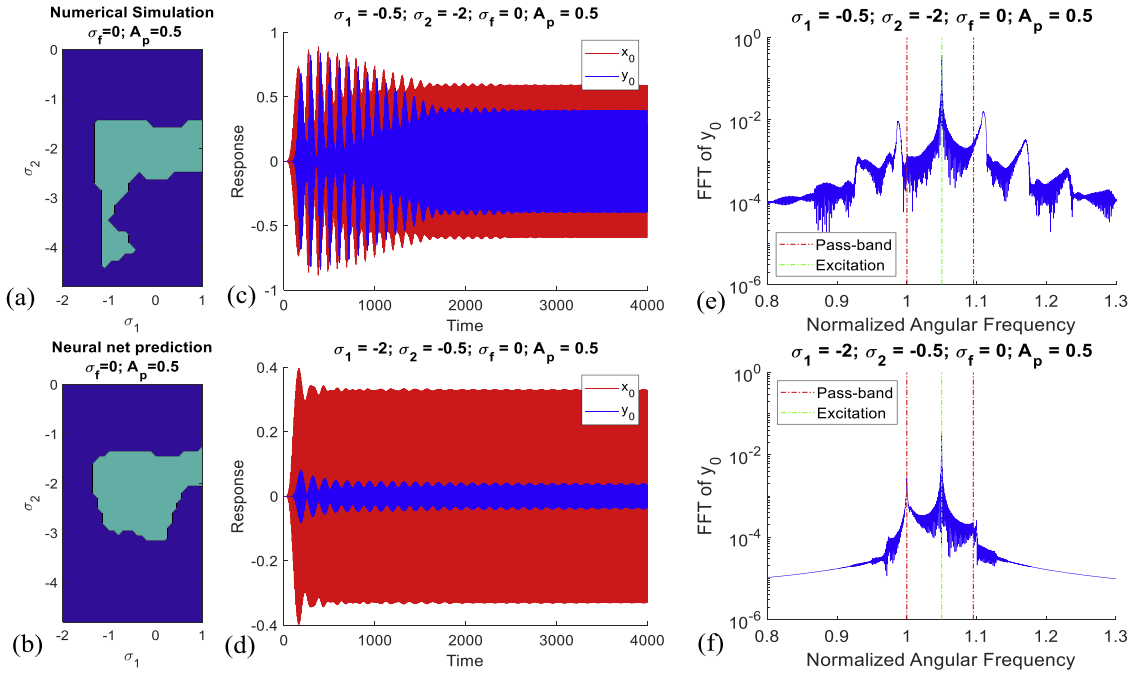

Fig. 13. Robust realization B for $(\sigma_f, A_p) = (0, 0.5)$: Region of good performance based on (a) direct numerical simulations of the equations of motion, and (b) NN predictions; (c,d) responses of the gate oscillators for $(\sigma_1, \sigma_2) = (-0.5, -2)$, and $(\sigma_1, \sigma_2) = (-2, -0.5)$, respectively, highlighting the acoustic non-reciprocity of the gated waveguide; and (e,f) corresponding Fourier transform spectrum of y_0 for (c) and (d), respectively.

Table 2
Performance measures of the gated waveguide for realizations A, B and C

Realization	A: $(\sigma_f, A_p, \sigma_1, \sigma_2) = (0, 0.25, -0.5, -2)$		B: $(\sigma_f, A_p, \sigma_1, \sigma_2) = (0, 0.5, -0.5, -2)$		C: $(\sigma_f, A_p, \sigma_1, \sigma_2) = (0.75, 0.55, -4.2, -0.2)$	
Measures	η	δ	η	δ	η	δ
NN output	0.018	1.663	0.390	2.158	0.220	2.400
Simulation	0.002	1.112	0.263	2.045	0.021	2.461

Based on the initial study with the coarse dataset, a second NN simulator is created based on a more compact (denser) dataset in the subregion defined by $\sigma_1 \in [-2, 1]$, $\sigma_2 \in [-4.8, 0]$, and with (σ_f, A_p) being consistent with the domain of the first NN simulator. The grid dataset is then generated, where A_p is uniformly distributed in the range $[0.2, 0.8]$ with an increment of 0.2, σ_1 is uniformly distributed in its range with an increment of 0.3, σ_2 is uniformly distributed in its range with an increment of 0.4, and the grid values for σ_f are still selected as $-0.9,\ -0.6,\ -0.3,\ 0,\ 0.2,\ 0.35,\ 0.5,\ 0.65$ and 0.85. Moreover, the second NN simulator for the denser dataset possesses a total of 5 layers with 50 neurons per layer (cf. Appendix B).

To evaluate the validity of the second NN, we compare its predicted transmissibility and the non-reciprocity measures predicted with the corresponding results from direct numerical simulations on the test set. These comparisons are shown in Fig. 11, where the correlations for both measures are ~ 0.99, which are much improved compared with the results of the first NN simulator for the coarse data set (cf. Fig. 9). Still, our previous definition of good (or desirable) performance for the gated waveguide holds, that is, when the non-reciprocity measure satisfies $\delta > 1$ and the transmissibility $\eta > 0.2$. In Table 1 we show the confusion matrix of the categorization. TP denotes the amount of true positive data that are found to be desirable by both the NN simulator and the direct numerical simulations; TN denotes the amount of true negative data, which are found to be undesirable both by the NN simulator and the direct numerical simulations; FP denotes the amount of false positive data that are found to be desirable by the NN simulator but undesirable by the direct numerical simulations; and lastly, FN denotes the amount of false negative data that are found to be undesirable by the NN simulator but desirable by the direct numerical simulations. The following measures are then formulated to evaluate the efficacy of the NN:

$$\text{Sensitivity} = \frac{\text{TP}}{\text{TP} + \text{FN}}, \quad \text{Specificity} = \frac{\text{TN}}{\text{TN} + \text{FP}}, \quad \text{Precision} = \frac{\text{TP}}{\text{TP} + \text{FP}} \tag{15}$$

The values of the sensitivity, specificity and precision for the predictions of the second NN are listed in Table 1. The sensitivity, precision and specificity measures are all close to unity, which indicates that the NN simulator captures well and with high accuracy the parameter ranges of good (desirable) performance. A parametric study of the sensitivity, specificity, and precision measures for

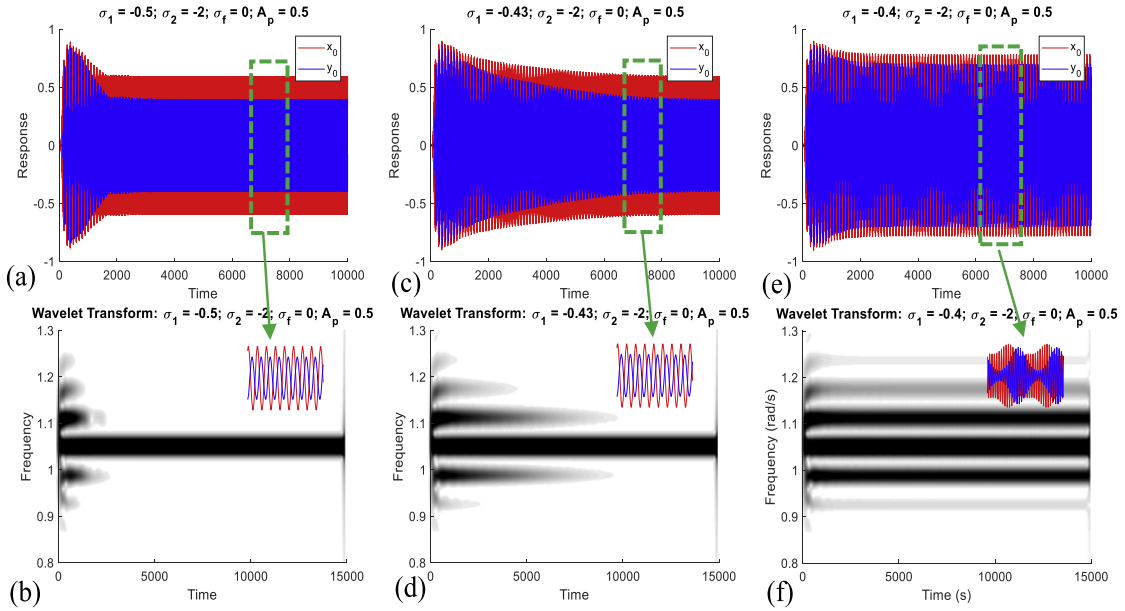

Fig. 14. The gate responses x_0 and y_0, and corresponding wavelet spectrum of y_0 for realization B with $(\sigma_2, \sigma_f, A_p) = (-2, 0, 0.5)$ and varying σ_1: (a, b) $\sigma_1 = -0.5$, (c,d) $\sigma_1 = -0.43$, and (e,f) $\sigma_1 = -0.4$; note the transition from monochromatic to SMR steady state response.

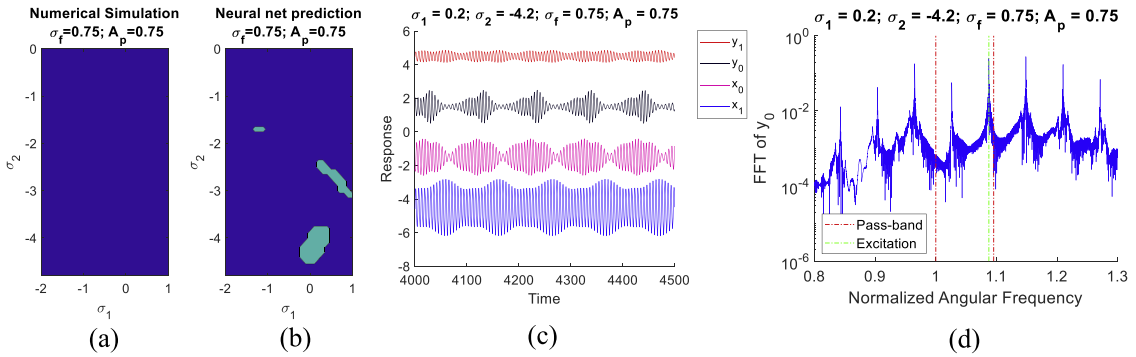

Fig. 15. Weakly robust realization C for $(\sigma_f, A_p) = (0.75, 0.75)$: Region of good performance based on (a) direct numerical simulations of the equations of motion, and (b) NN predictions; (c) responses of the gate and two neighboring oscillators for $(\sigma_1, \sigma_2) = (-4.2, 0.2)$, and (d) the corresponding Fourier spectrum of y_0.

varying numbers of neurons/layer and total number of layers is shown in Appendix C, confirming the architecture of the NN for best classification performance.

Now we proceed to a visualization of the results of the previous two steps of performance optimization. This is a challenging task as the parameter space is four dimensional. To address this challenge, we introduce an auxiliary measure, the *kernel size*, which is defined by fixing two of the parameters at a time. In particular, in Fig. 12a the region of desirable performance (corresponding to $\eta > 0.2$ and $\delta > 1$) is depicted in the (σ_1, σ_2) for fixed values of $\sigma_f = 0$ and $A_p = 0.5$. Then, we fit a square to this region, whose side length we refer to as the kernel size of the region of good performance for the specific fixed values of σ_f and A_p. Therefore, the kernel size can be regarded as a robustness measure of the region of good performance for a given a set of fixed values of (σ_f, A_p). The variation of the kernel size for varying values of (σ_f, A_p) is then depicted in Fig. 12b, from which we infer two regions of good performance for the gated waveguide. The major region is realized for $\sigma_f \approx 0$ and extends up to large values of A_p in the approximate range $[0.5, 0.8]$, whereas the minor (and less robust) region corresponds to a vertical strip with $\sigma_f \in [0.6, 0.8]$ and $A_p \in [0.5, 0.8]$. In these regions, especially in the central major one, the good performance of the gated waveguide is robust to the variation of the four considered parameters; whereas, in the minor region the kernel size is generally smaller compared to the major one, indicating weaker robustness.

Based on the optimization results of Fig. 12 we will examine in more detail certain realizations of the nonlinear gated waveguide in order to highlight its non-reciprocity and transmissibility features. Specifically, we will consider the three realizations denoted by crosses in Fig. 12b, which we will denote as, realization A with $(\sigma_f, A_p) = (0, 0.25)$ (non-robust), realization B with $(\sigma_f, A_p) = (0, 0.5)$ (robust) and realization C with $(\sigma_f, A_p) = (0.75, 0.75)$ (weakly robust). Realization A is a case of non-robustness since it corresponds to

a small kernel size in the (σ_1, σ_2) plane, whereas the other two realizations are more robust since they correspond to larger kernel sizes, with realization B being predicted as being the most robust. Accordingly, to each realization we can associate a plot of predicted good performance in the (σ_1, σ_2) plane (analogous to the one shown in Fig. 12a), which can assist us in exploring the steady state acoustics for different combinations of the detuning parameters of the gate.

In Fig. 13 we present the results for the robust realization B corresponding to $(\sigma_f, A_p) = (0, 0.5)$ and $(\sigma_1, \sigma_2) = (-0.5, -2)$ and $(-2, -0.5)$. We iterate here that flipping the values of σ_1 and σ_2 is equivalent to inter-changing the site of the applied harmonic excitation between the left and right sub-waveguides; hence, this flipping is used to study acoustic non-reciprocity in the gated waveguide. In Figs. 13a and 13b we compare the regions of good performance in the (σ_1, σ_2) plane as predicted by direct numerical simulations and the NN, respectively, and note that NN manages to well capture the numerical integration results. The resulting non-reciprocity and transmissibility measures are listed in Table 2, again validating the predictive capacity of the NN, especially for the non-reciprocity measure. The simulation results for the gated waveguide corresponding to $(\sigma_1, \sigma_2) = (-0.5, -2)$ are shown in Figs. 13c and 13e, whereas the ones for the flipped values of σ_1 and σ_2 in Figs. 13d and 13f. Large disparity in the responses x_0 and y_0 of the gate oscillators is observed when the excitation is flipped, verifying the strong non-reciprocity in the nonlinear acoustics. Moreover, from Fig. 13c we note that the responses x_0 and y_0 are strongly modulated in the transient stage (i.e., following the application of the harmonic excitation), whereas they reach constant-amplitude steady state oscillations. This indicates that for this realization the system reaches a monochromatic steady state, and so the secondary peaks in the Fourier spectrum shown in Fig. 13e results from the transient acoustics. Similar conclusions can be drawn from the responses depicted in Figs. 13d and 13f.

To prove the robustness of the steady state response in realization B, in Fig. 14 we plot the Morlet wavelet transform spectrum of the response y_0 of the gate oscillator for $(\sigma_2, \sigma_f, A_p) = (-2, 0.5, 0)$ and three different detuning values $\sigma_1 = -0.4, -0.43$ and -0.5. For $\sigma_1 = -0.5$ (cf. Figs. 14a,b), only one harmonic component survives at steady state, and this corresponds to the excitation frequency shown in Fig. 13e. In this case, the gated waveguides exhibits strong non-reciprocity and transmissibility with *no frequency conversion* at the steady state; that is, the "input signal" that impedes to the nonlinear gate from the upstream sub-waveguide, has the same frequency with the "output signal" transmitted to the downstream sub-waveguide. The effect of slightly reducing the detuning σ_1 is showed in Figs. 14c-f, where, through the emergence of additional harmonic components, a transition from a monochromatic (for $\sigma_1 = -0.5$) to an SMR (for $\sigma_1 = -0.4$) steady state response. Yet, the transmissibility (and non-reciprocity – not depicted in Fig. 14) are still preserved even in the presence of multiple harmonics and the corresponding qualitative change in the steady state response.

In Fig. 15 we consider the weakly robust realization C with $(\sigma_f, A_p) = (0.75, 0.75)$. We start by comparing the regions of good performance predicted by direct numerical simulations (Fig. 15a) and the NN (Fig. 15b). Based on the direct numerical simulations, the steady state responses do not meet the transmissibility and non-reciprocity thresholds for good performance for varying detuning parameters σ_1 and σ_2; in contrast, several narrow regions of good performance are predicted by the NN, which, still confirms the weakly robust feature of the waveguide performance in this case. Selecting $(\sigma_1, \sigma_2) = (-4.2, 0.2)$ in the region of good performance as predicted by the NN, in Fig. 15c we depict the steady state responses of the gate oscillators x_0, y_0 and the neighboring oscillators x_1, and y_1. We note the modulated character of the responses in this case, which is confirmed by the multi-frequency Fourier spectrum of y_0 in Fig. 15d. From these results we note that as the wave passes through the nonlinear gate, the response amplitudes decrease implying a small transmissibility ratio. This indicates that an SMR response for a gate oscillator is not a sufficient condition for good performance of the gated waveguide. Moreover, from Table 2 we note that for this realization the numerical transmissibility measure $\eta = 0.021$ is much smaller than the one predicted by the NN, $\eta = 0.220$. In addition, from Table 1 the precision of the prediction is 0.918, which means that with ~8.2% of non-desirable response predicted by the NN, proves to be desirable in the direct numerical simulations. From these results we deduce that the predictions concerning the region of good performance for the weakly robust realization C are not reliable and only robust realizations (e.g., realization B) should be considered for reliable predictions of the NN.

Lastly, in Figs. 16a and 16b, we consider the regions of good performance predicted by direct numerical simulations and the NN, respectively, for the non-robust realization A with $(\sigma_f, A_p) = (0.25, 0)$. In this case both predictions confirm that the steady state responses do not meet the thresholds for good performance as σ_1 and σ_2 vary. In Fig. 16c we depict the steady state responses of the gate oscillators for $(\sigma_1, \sigma_2) = (-0.5, -2)$, whereas in Fig. 16d we show the corresponding Fourier spectrum of y_0. In this case the steady state responses are monochromatic, and the transmissibility through the nonlinear gate is small. From Table 2, it holds that for this realization the transmissibility η is far below the (good performance) threshold of 0.2, and this is confirmed by both direct numerical simulations and the NN.

These results conclude our study of the performance of the non-reciprocal gated waveguide based on machine learning. In synopsis, the developed trained NN simulator well captures and predicts the performance of the gated waveguide. This is verified through by correlating the predicted and actual performance measures, creating a confusion matrix, and directly comparing the predictions of the NN simulator and direct numerical simulations of the governing equations of motion. Based on the predictions of the NN simulator, a robust region of good performance (in terms of both non-reciprocity and transmissibility) was detected, which, in turn, can be directly employed for the predictive design of the gated waveguide with robust non-reciprocity features. In the process we deduced that steady state SMRs (that involve strong frequency conversion of waves transmitted through the nonlinear gate) are not the only way to achieve non-reciprocity. Indeed, a robust non-reciprocal gated waveguide can also be designed for monochromatic wave transmission downstream, which, interesting enough, has the added benefit of the absence of frequency conversion, i.e., distortion of the signal transmitted downstream through the nonlinear gate.

5. Concluding remarks

A machine-based approach was developed to explore the break of classical acoustic reciprocity in an infinite one-dimensional linear

waveguide incorporating a local nonlinear gate with cubic stiffness nonlinearity and configurational asymmetry. The local gate divides the waveguide into linear sub-waveguides, namely an upstream one (where the harmonic excitation is applied) and a downstream one. A specific characteristic of the (ungated) linear waveguide is that it consists of an infinite number of identical grounded oscillators that are coupled through weak coupling, and as a result its single pass band is narrow; as a result, the ungated waveguide supports narrowband wave transmission in its far field. Only excitation frequencies inside the pass band were considered in our study since only such excitations generate waves that can reach the local gate and transmit through it downstream.

A complexification-averaging analysis based on slow-fast partition of the acoustical responses predicted that there are two classes of steady state acoustics in the gated waveguide, namely monochromatic responses, and strongly modulated responses (SMRs). Due to the combined stiffness nonlinearity and structural asymmetry of the *local* gate, both classes of responses may yield strong non-reciprocity in the *global* steady state acoustics. Both the strength and robustness of the achieved acoustic non-reciprocity, which is energy-dependent due to the gate nonlinearity, can be tuned simply through the design of a local gate. Moreover, this non-reciprocity can be achieved either with *strong frequency distortion* of the transmitted signal through the nonlinear gate (for SMRs) or *no frequency distortion* (for monochromatic responses); in that latter case both the input and output signals at the gate are dominated by the excitation frequency since any other generated harmonics lie outside the pass band of the waveguide and so are near-field. These features highlight the high degree of passive tunability (with respect to energy, frequency content, and robustness – as discussed below) of the global acoustics of this system achieved by the simple incorporation of a single local gate.

In this study, the performance of the gated waveguide was deemed to be good if certain thresholds ensuring satisfactory non-reciprocity and transmissibility through the gate were met. Employing this criterion we optimized the performance by constructing two NNs based learnable simulators which were designed to predict (i) the frequencies and amplitudes of the harmonics of the transmitted wave through the gate, and (ii) the overall transmissibility and non-reciprocity features (measured by certain metrics) of the gated waveguide. The first NN simulator allows us to predict the harmonics efficiently for fixed excitation and variable gate detuning parameters (affecting the configurational asymmetry of the gate); the second NN enabled the prediction of the transmissibility and non-reciprocity in the steady state acoustics. Different NNs were considered in this study, based on different architectures, i.e., number of layers and neurons per layer. The applications of the learnable simulators drastically reduce the required simulation times, which enables the design and optimization of the gated waveguide more efficiently. Our study reveals a robust region of good performance in a four-dimensional parameter space, ensuring strong transmissibility and acoustic non-reciprocity. Selected direct numerical simulations validated the NN predictions.

The machine learning approach discussed here paves the way for non-reciprocity studies of the acoustics of practical waveguides with finite boundaries and with one or more local nonlinear "inclusions", i.e., local structural modifications acting, in essence, as nonlinear gates. The theoretical models and the design rules discussed in this work has possible applications in experimental setups in both macro-scale [17] and nano-scale [27]. Moreover, the approach can be extended for strongly coupled waveguides (which is the topic of current research by the authors) as well, but also to higher dimensions, e.g., two- or three-dimensional linear waveguides incorporating local nonlinear gates. Moreover, the approach is fully scalable across scales, and as such it can be extended to phononic lattice systems in the micro-scale, e.g., providing practical ways for inducing features of acoustic non-linear non-reciprocity in systems of coupled passive MEMS resonators.

CRediT authorship contribution statement

C. Wang: Conceptualization, Methodology, Formal analysis, Software, Visualization, Writing – original draft. **A. Mojahed:** Methodology, Software, Writing – review & editing. **S. Tawfick:** Supervision, Project administration, Conceptualization, Formal analysis, Resources, Writing – review & editing. **A. Vakakis:** Supervision, Project administration, Conceptualization, Formal analysis, Resources, Writing – review & editing.

Declaration of Competing Interest

The authors declare that they have no known competing financial interests or personal relationships that could have appeared to influence the work reported in this paper.

Data availability

No data was used for the research described in the article.

Acknowledgement

This work was supported in part by NSF Emerging Frontiers Research Initiative (EFRI) Grant 1741565. This support is gratefully acknowledged. Also, we would like to acknowledge the useful discussions on the contents of the paper with Ali Kanj at the University of Illinois at Urbana – Champaign.

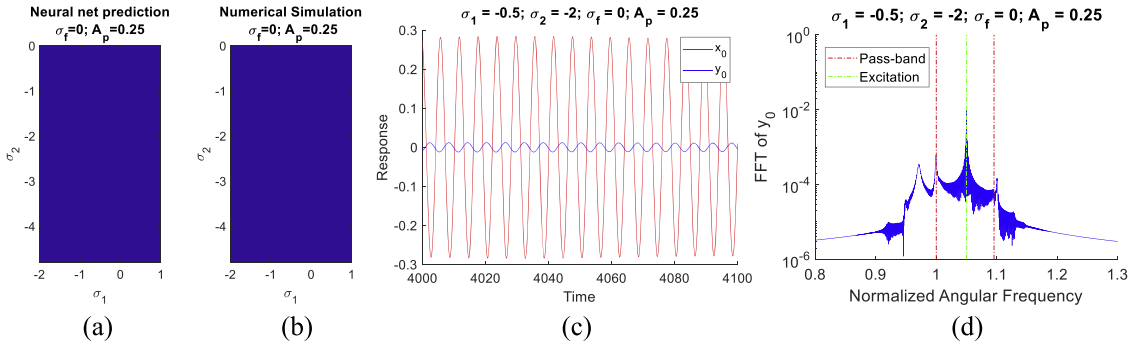

Fig. 16. Non-robust realization A for $(\sigma_f, A_p) = (0, 0.25)$: Region of good performance based on (a) direct numerical simulations of the equations of motion, and (b) NN predictions; (c) responses of the gate oscillators for $(\sigma_1, \sigma_2) = (-0.5, -2)$, and (d) the corresponding Fourier spectrum of y_0

Appendix A. Green's function of the infinite linear waveguide and some details of the multiple-scales analysis of section 2

The Green's function G_m in (3) of the infinite, weakly coupled waveguide,

$$u_n'' + u_n + \varepsilon D(u_n - u_{n-1}) + \varepsilon D(u_n - u_{n+1}) = 0, -\infty < n < +\infty \tag{A-1}$$

is explicitly given by [22],

$$G_m = \frac{1}{\pi}\int_0^{\pi} \frac{\cos(m\theta)}{\omega(\theta)} \sin[\omega(\theta)\tau] d\theta \tag{A-2}$$

where θ denotes the wave number and ω the corresponding (normalized) frequency given by:

$$\omega(\theta) = \sqrt{1 + 4\varepsilon D \sin^2(\theta/2)} = 1 + 2\varepsilon D \sin^2\left(\frac{\theta}{2}\right) + O(\varepsilon^2) \tag{A-3}$$

By definition, the Green's function (A-2) denotes the response u_{n+m} of the $(n+m) - th$ oscillator subject to a unit impulse applied to the $n - th$ oscillator, with no other excitations applied and zero initial conditions. Note that due to translational invariance the Green's function is independent of n, and satisfies the condition $G_m = G_{-m}$ due to symmetry.

Substituting (A-3) into (A-2) we obtain the following approximate slow-fast time scale partition for the Green's function:

$$G_m = -\frac{\mathrm{i}}{\pi}\int_0^{\pi} \cos(m\theta) e^{2iD\sin^2\left(\frac{\theta}{2}\right)\varepsilon\tau} d\theta \mathrm{e}^{\mathrm{i}\tau} + \mathrm{cc} + O(\varepsilon) = g_m(\tau_1)\mathrm{e}^{\mathrm{i}\tau_0} + \mathrm{cc} + O(\varepsilon) \tag{A-4}$$

Note that this partition is made possible by our assumption of narrow pass band of the waveguide (i.e., weak coupling), which enables the existence of a single dominant fast component in the response at a normalized (fast) frequency equaling unity. Hence, the analysis is formulated under the assumption that there exists *a fast time scale* $\tau_0 = \tau$ and *a slow time scale* $\tau_1 = \varepsilon\tau$ in the Green's function and the waveguide responses.

Next, we proceed to analyze the leading order approximations for the convolution products in (3), given the fast-slow separation of variables in (A-4). As an example we consider in detail the term $\varepsilon^2 D^2 x_0 * G_m$ which, taking into account the multiple-scale analysis in Section 2, is expressed in terms of a slow-fast time scale partition as follows:

$$\varepsilon^2 D^2 x_0 * G_m = \varepsilon D^2 [X_0(\tau_1) * g_m(\tau_1)]\mathrm{e}^{\mathrm{i}\tau_0} + \mathrm{cc} + O(\varepsilon^2) \tag{A-5}$$

We note that the fast frequencies of x_0 and G_m are the same (as expected). Therefore, the convolution of these two series still admits fast-slow separation of time scales. Moreover, due to the assumption of 1:1 resonance and the change of time scales of the convolution, one of the small factors ε is absorbed in the convolution product itself. Similarly, it can be proven that all convolution products at the right-hand side of (4) are $O(\varepsilon)$ terms. Therefore, the $O(\varepsilon)$ expansion of (4) is given by,

$$\frac{\partial^2 x_{01}}{\partial \tau_0^2} + x_{01} + \alpha D\left\{\left[X_{00}(\tau_1) - Y_{00}(\tau_1)\right]e^{i\tau_0} + cc\right\}^3 = -2\frac{\partial}{\partial \tau_0}\left(\frac{\partial X_{00}(\tau_1)e^{i\tau_0}}{\partial \tau_1}\right)$$
$$+(1+\sigma_1+2i\zeta)DX_{00}(\tau_1)e^{i\tau_0} + \varepsilon D^2\{X_{00}(\tau_1) * [g_0(\tau_1) - g_2(\tau_1)]\}e^{i\tau_0}$$
$$+D^2\left\{A_p e^{iD(1+\sigma_f)\tau_1} * \left[g_{p-1}(\tau_1) - g_{p+1}(\tau_1)\right]\right\}e^{i\tau_0} + cc \tag{A-6}$$
$$\frac{\partial^2 y_{01}}{\partial \tau_0^2} + y_{01} + \alpha D\left\{\left[Y_{00}(\tau_1) - X_{00}(\tau_1)\right]e^{i\tau_0} + cc\right\}^3 = -2\frac{\partial}{\partial \tau_0}\left(\frac{\partial Y_{00}(\tau_1)e^{i\tau_0}}{\partial \tau_1}\right)$$
$$+(1+\sigma_2+2i\zeta)DY_{00}(\tau_1)e^{i\tau_0} + \varepsilon D^2\{Y_{00}(\tau_1) * [g_0(\tau_1) - g_2(\tau_1)]\}e^{i\tau_0} + cc$$

Lastly, we note that the slow part, g_m, of the Green's function G_m can be expressed alternatively in terms of the Bessel function J_m as follows,

$$g_m = -\frac{i}{2\pi}\int_0^{\pi}\cos(m\theta)e^{-iD\tau_1 cos\ \theta}d\theta e^{iD\tau_1} = \frac{1}{2}(-i)^{n+1}J_m(D\tau_1)e^{iD\tau_1} \tag{A-7}$$

Therefore, the slow flow modulation Eq. (7) can be derived by substituting (A-7) into (A-6) and eliminating the secular terms in (A-6) (i.e., the coefficient multiplying the fast term $e^{i\tau_0}$).

Appendix B. Construction and training of the neural network of Section 3

In the simulation data set, the input and output variables are assembled into a 2×1 vectors and 20×1 vectors, respectively. The input variables are the detuning parameters (σ_1,σ_2), while the output variables are the frequencies and amplitudes identified from the simulation results $(\omega_i,E(\omega_i))$. The first 10 elements of the output vector are the frequencies ω_i sorted in the ascending order, while the last 10 elements are the corresponding amplitudes $E(\omega_i)$. Moreover, in each simulation, we identify the frequencies and amplitudes, ω_i and $E(\omega_i)$, respectively, of the corresponding Fourier spectrum (which are the output of the NN). Note that the size of the output vector varies in the dataset, since not all 1681 sets of data will possess 10 peaks in the Fourier spectrum. Hence, to match the sizes of all output vectors, in cases where less than 10 peaks exist we complement them (up to 10) with artificial peaks at frequencies $\omega_i = 1$ and amplitudes $E(\omega_i) = 0$. Therefore, each output vector consists of 10 frequency components and 10 corresponding amplitudes. Moreover, each individual element of the input and the output vectors is linearly mapped in the range $[-1,1]$, by normalizing the maximum element to 1 and the minimum to - 1.

Considering the architecture of the NN, it is constructed and trained using the MATLAB deep learning toolbox. In this work, we use two hidden layers with twenty neurons in each layer to train the NN, whose schematic is depicted in Fig. B-1. Denoting the input vector as X_0, the output vector as Y, and the vector of the $n-th$ hidden layer as X_n, since there are 20 neurons in each hidden layer, the vectors of the hidden layers are 20×1 as well. The value of each layer is mapped from the previous layer with a composite transformation, consisting of a linear and a nonlinear transformation with activation functions given by,

$$\begin{aligned} X_i &= f(w_i X_{i-1} + b_i) \\ Y &= g(w_{n+1}X_n + b_{n+1}) \end{aligned} \tag{B-1}$$

where f and g denote the activation functions of the hidden and the output layers, respectively; w_i and b_i denote the matrices and vectors composed of learnable coefficients. In this work, the activation function of the output layer is the identity transformation, while the activation function of the hidden layers is the *ReLU* function given by:

$$f(x) = \begin{cases} x & (x > 0) \\ 0 & (x \le 0) \end{cases} \tag{B-2}$$

For the training of the NN, the mean square error is adopted as its performance function. The Levenberg Marquardt back propagation algorithm is adopted to train the weights w_i and b_i in the NN in order to minimize the performance function. The dataset is randomly divided into three subsets, with 50% assigned for training, 15% for validation and 35% for testing. Only the training parameters are used to train the weights and optimize the performance function. An epoch is defined as a complete pass of the training set. The performance function in the validation subset is evaluated after each epoch, and the training stops after 6 epochs of increased error rate in the validation is reached, to avoid overfitting. In order to evaluate the performance of the trained NN simulator on the

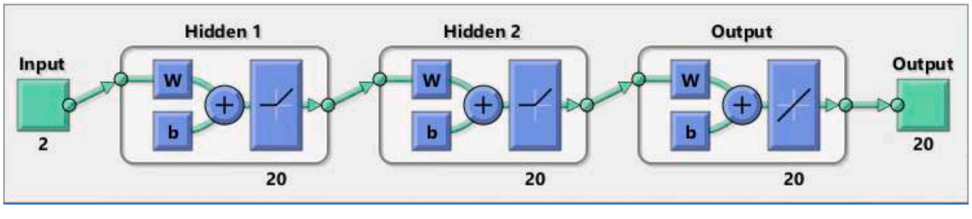

Fig. B-1. Schematic showing the architecture of the NN.

entire parameter domain of interest, we compare the outputs of the NN simulator with the original numerical simulation, as shown in Fig. 5; this comparison is based on the part of the test set that does not participate in the training process.

Note that the NN simulator cannot distinguish between physical and low-amplitude artificial (spurious) peaks. From Fig. 5, we note that the correlation between the NN prediction and the physical simulation is high. Therefore, we expect that the output prediction of small artificial peaks does not affect the accuracy of the predicted averaged downstream power (12) and the non-reciprocity (11). However, it is still important to distinguish between the physical and artificial peaks in the predicted output to identify accurately the types of the steady-state acoustics. To this end, we distinguish the artificial peaks from the physical peaks from their amplitudes. For each output vector, a threshold is set as 1% of the maximum amplitude of the peaks: All peaks with amplitudes above the threshold are identified as physical peaks, otherwise they are neglected as artificial peaks. The predicted number of peaks is plotted in Fig. 6c and the contour denotes the amounts of identified physical peaks in the output given an arbitrary input (σ_1, σ_2).

We claim that the NN simulator drastically saves the simulation time and memory, which allows us to study the waveguide response at high-dimensional parametric domains. Note that the time complexity of a trained NN simulator is proportional to the number of hidden layers. Each layer possesses a composite transformation whose time complexity is proportional to the square of the numbers of neurons. Meanwhile, the time complexity of the direct numerical simulation is proportional to the number of state variables and the simulation time steps. In the direct simulations, there are 2000 state variables in total (the displacements and velocities for each oscillator) and 150,000 time step intervals. This is replaced by a NN simulator with only 2 hidden layers with 20 neurons per layer. Based on the analysis, the time complexity is reduced by around five orders of magnitude. We compare the simulation time of the NN simulator developed in Section 3 and direct simulation for $(\sigma_1, \sigma_2) = (1, 0)$ with the other parameters fixed to $\varepsilon = 0.05$, $\zeta = 0.05$, $\sigma_f = 0.5$, $D = 1$, $\alpha = 2$ and $A_p = 0.25$. Using the same computing server, the simulation time for the NN simulator is around 2.56*ms*, while the direct simulation takes around 69.0*s*. It is observed that the simulation time is reduced by around 4 to 5 orders of magnitude, which agrees with the time complexity analysis and enables us to efficiently conduct the parametric study.

Appendix C. Parametric study of the neural network for the dense dataset in section 4

Here we investigate the predictive capacity of the NN developed for the dense set for varying layers and neurons per layer. To this end, multiple NN simulators were trained composed of 2 to 10 layers, and with 20 to 70 neurons per layer. The resulting sensitivity, specificity, precision, and correlations for the transmissibility and non-reciprocity measures between the NN predictions and the direct numerical integrations are listed in Tables C1–C5. We notice that the specificity and correlations are all close to 0.99, however, the sensitivity and precision performance varies. Therefore, we conclude that the best overall performance is achieved by the NN containing 50 layers and 5 neurons per layer, which is chosen as the simulator for the dense data set in section 4.

Table C1
The sensitivity of the NN prediction.

Layers/Neurons	2	3	4	5	6	7	8	9	10
20	0.717	0.796	0.647	0.768	0.782	0.628	0.713	0.738	0.459
30	0.717	0.800	0.798	0.789	0.752	0.689	0.769		
40	0.850	0.856	0.833	0.771	0.529	0.813	0.505		
50	0.722	0.759	0.840	0.878	0.750	0.805			
60	0.852	0.850	0.848	0.752					
70	0.817	0.848	0.843	0.774					

Table C2
The specificity of the NN prediction.

Layers/Neurons	2	3	4	5	6	7	8	9	10
20	0.995	0.994	0.993	0.995	0.989	0.996	0.988	0.995	0.988
30	0.992	0.995	0.995	0.994	0.993	0.995	0.990		
40	0.995	0.997	0.997	0.994	0.994	0.993	0.987		
50	0.988	0.992	0.994	0.996	0.994	0.993			
60	0.995	0.992	0.993	0.992					
70	0.992	0.995	0.997	0.997					

Table C3
The precision of the NN prediction.

Layers/Neurons	2	3	4	5	6	7	8	9	10
20	0.864	0.854	0.828	0.869	0.767	0.877	0.748	0.864	0.646
30	0.800	0.875	0.892	0.869	0.850	0.866	0.761		
40	0.889	0.931	0.924	0.867	0.831	0.858	0.639		
50	0.722	0.838	0.873	0.918	0.870	0.864			
60	0.885	0.827	0.886	0.806					
70	0.847	0.888	0.944	0.921					

Table C4
The correlation for the transmissibility between the NN prediction and the direct numerical simulations for the dense data set.

Layers/Neurons	2	3	4	5	6	7	8	9	10
20	0.974	0.982	0.975	0.987	0.985	0.977	0.974	0.987	0.951
30	0.980	0.983	0.990	0.991	0.988	0.984	0.988		
40	0.986	0.989	0.989	0.988	0.948	0.984	0.916		
50	0.944	0.986	0.993	0.993	0.979	0.983			
60	0.986	0.990	0.988	0.985					
70	0.964	0.988	0.992	0.988					

Table C5
The correlation of the non-reciprocity between the NN prediction and the direct numerical simulations for the dense data set.

Layers/Neurons	2	3	4	5	6	7	8	9	10
20	0.978	0.982	0.982	0.983	0.983	0.979	0.987	0.988	0.972
30	0.983	0.985	0.992	0.989	0.992	0.992	0.991		
40	0.990	0.989	0.992	0.987	0.971	0.985	0.965		
50	0.977	0.991	0.992	0.994	0.989	0.988			
60	0.989	0.993	0.990	0.991					
70	0.979	0.992	0.995	0.991					

References

[1] J. Achenbach, Reciprocity in Elastodynamics, Cambridge University Press, Cambridge, UK, 2009.
[2] K. Tsakmakidis, L. Shen, S. Schulz, X. Zheng, J. Upham, X. Deng, H. Altug, A. Vakakis, R.W. Boyd, Breaking Lorentz reciprocity to overcome the time-bandwidth limit in physics and engineering, Science 356 (6344) (2017) 1260–1264.
[3] R. Fleury, D. Sounas, C. Sieck, M. Haberman, A. Alù, Sound isolation and giant linear nonreciprocity in a compact acoustic circulator, Science 343 (6170) (2014) 516–519.
[4] S. Cummer, Selecting the direction of sound transmission, Science 343 (6170) (2014) 495–496.
[5] R. Fleury, D. Sounas, A. Alù, Subwavelength ultrasonic circulator based on spatiotemporal modulation, Phys. Rev. B 91 (17) (2015), 174306.
[6] S.A. Cummer, J. Christensen, A. Alù, Controlling sound with acoustic metamaterials, Nat. Rev. Mater. 1 (3) (2016) 1–13.
[7] A.A. Maznev, A.G. Every, O.B. Wright, Reciprocity in reflection and transmission: What is a 'phonon diode'? Wave Motion 50 (4) (2013) 776–784.
[8] B. Liang, X.S. Guo, J. Tu, D. Zhang, J.C. Cheng, An acoustic rectifier, Nat. Mater. 9 (12) (2010) 989–992.
[9] C. Fu, B. Wang, T. Zhao, C.Q. Chen, High efficiency and broadband acoustic diodes, Appl. Phys. Lett. 112 (5) (2018), 051902.
[10] H. Nassar, Y. Behrooz, F. Romain, R. Massimo, A. Andrea, D. Chiara, N.N. Andrew, H. Guoliang, H.R. Michael, Nonreciprocity in acoustic and elastic materials, Nat. Rev. Mater. 5 (9) (2020) 667–685.
[11] A. Blanchard, T.P. Sapsis, A.F. Vakakis, Non-reciprocity in nonlinear elastodynamics, J. Sound Vib. 412 (2018) 326–335.
[12] S. Lepri, C. Giulio, Asymmetric wave propagation in nonlinear systems, Phys. Rev. Lett. 106 (16) (2011), 164101.
[13] Q. Zhang, W. Li, J. Lambros, L. Bergman, A. Vakakis, Pulse transmission and acoustic non-reciprocity in a granular channel with symmetry-breaking clearances, Granular Matter 22 (1) (2020) 1–16.
[14] J.G. Cui, T. Yang, L.Q. Chen, Frequency-preserved non-reciprocal acoustic propagation in a granular chain, Appl. Phys. Lett. 112 (18) (2018), 181904.
[15] C. Wang, S. Tawfick, A.F. Vakakis, Time scale disparity yielding acoustic nonreciprocity in a two-dimensional granular-elastic solid interface with asymmetry, Phys. Rev. E 104 (4) (2021), 044906.
[16] I. Grinberg, A.F. Vakakis, O.V. Gendelman, Acoustic diode: Wave non-reciprocity in nonlinearly coupled waveguides, Wave Motion 83 (2018) 49–66.
[17] A. Darabi, L. Fang, A. Mojahed, M.D. Fronk, A.F. Vakakis, M.J. Leamy, Broadband passive nonlinear acoustic diode, Phys. Rev. B 99 (21) (2019), 214305.
[18] S. He, Y. Li, F. Yu, S. Ho, S. Ravanbakhsh, W. Chen, B. Póczos, Learning to predict the cosmological structure formation, Proc. Natl. Acad. Sci. 116 (28) (2019) 13825–13832.
[19] L. Ladický, S. Jeong, B. Solenthaler, M. Pollefeys, M. Gross, Data-driven fluid simulations using regression forests, ACM Trans. Graphics (2015).
[20] A.S. Gonzalez, J. Godwin, T. Pfaff, R. Ying, J. Leskovec, P.W. Battaglia, Learning to simulate complex physics with graph networks, in: International Conference on Machine Learning, 2020.
[21] Y.Y. Wang, K.H. Lee, Propagation of a disturbance in a chain of interacting harmonic oscillators, Am. J. Phys. 41 (1) (1973) 51–54.
[22] A.F. Vakakis, M.A. Al-Shudeifat, M.A. Hasan, Interactions of propagating waves in a one-dimensional chain of linear oscillators with a strongly nonlinear local attachment, Meccanica 49 (10) (2014) 2375–2397.
[23] A. Nayfeh, D. Mook, Nonlinear Oscillations, Wiley Interscience, New York, 1985.
[24] J. Bunyan, K. Moore, A. Mojahed, M. Fronk, M. Leamy, S. Tawfick, A. Vakakis, Acoustic nonreciprocity in a lattice incorporating nonlinearity, asymmetry, and internal scale hierarchy: Experimental study, Phys. Rev. E 97 (5) (2018), 052211.
[25] C. Wang, S. Tawfick, A.F. Vakakis, Irreversible energy transfer, localization and non-reciprocity in weakly coupled, nonlinear lattices with asymmetry, Physica D 402 (2020), 132229.
[26] A. Vakakis, M. Raheb, C. Cetinkaya, Free and forced dynamics of a class of periodic elastic systems, J. Sound Vib. 172 (1) (1994) 23–46.
[27] D. Hatanaka, I. Mahboob, K. Onomitsu, H. Yamaguchi, Phonon waveguides for electromechanical circuits, Nat. Nanotechnol. 9 (7) (2014) 520–524.